EXPERIMENTAL TWO-PHASE FLOW CHARACTERIZATION OF SUBCOOLED BOILING IN A RECTANGULAR CHANNEL

A Thesis

by

CARLOS EDUARDO ESTRADA PEREZ

Submitted to the Office of Graduate Studies of
Texas A&M University
in partial fulfillment of the requirements for the degree of

MASTER OF SCIENCE

May 2009

Major Subject: Mechanical Engineering

EXPERIMENTAL TWO-PHASE FLOW CHARACTERIZATION OF SUBCOOLED BOILING IN A RECTANGULAR CHANNEL

A Thesis

by

CARLOS EDUARDO ESTRADA PEREZ

Submitted to the Office of Graduate Studies of
Texas A&M University
in partial fulfillment of the requirements for the degree of

MASTER OF SCIENCE

Approved by:

Chair of Committee,	Yassin A. Hassan
Committee Members,	Kalyan Annamalai
	William H. Marlow
	Sy-Bor Wen
Head of Department,	Dennis L. O′Neal

May 2009

Major Subject: Mechanical Engineering

ABSTRACT

Experimental Two-Phase Flow Characterization
of Subcooled Boiling in a Rectangular Channel. (May 2009)
Carlos Eduardo Estrada Perez, B.S., Universidad Autónoma Metropolitana
Chair of Advisory Committee: Dr. Yassin A. Hassan

On the efforts to provide a reliable source of experimental information on turbulent subcooled boiling flow, time resolved Particle Tracking Velocimetry (PTV) experiments were carried out using HFE-301 refrigerant flow through a vertical rectangular channel with one heated wall. Measurements were performed at liquid Reynolds numbers of 3309, 9929 and 16549 over a wall heat flux range of 0.0 to 64.0 kW/m^2. From the PTV measurements, liquid two dimensional turbulence statistics are available, such as: instantaneous 2-D velocity fields, time-averaged axial and normal velocities, axial and normal turbulence intensities, and Reynolds stresses. The present results agree with previous works and provide new information due to the 2-D nature of the technique, for instance, this work shows that by increasing heat flux, the boiling bubbles influence on the liquid phase is portrayed as a persistent increase of axial velocity on regions close to the heater wall. This persistent increase on the axial velocity reaches a maximum value attributed to the terminal bubble velocity. These new observed phenomena must be considered for the development and improvement of two-phase flow turbulence models. To this end, an extensive error analysis was also performed with emphasis on the applicability of the PTV measurement technique on optically inhomogeneous flows. The error quantification exhibited negligible optically induced errors for the current conditions, making the data acquired in this work a vast and reliable source.

TABLE OF CONTENTS

CHAPTER Page

LIST OF TABLES

LIST OF FIGURES

FIGURE Page

CHAPTER I

INTRODUCTION

Turbulent subcooled boiling flow has been used extensively in industry because it is one of the most efficient heat transfer modes. The continuous mixing and stirring of liquid produced on the life cycle of the subcooled boiling bubbles (nucleation, growth, wall detachment, coalescence and collapsing) are local enhancing mechanisms of heat and momentum transfer. Therefore, liquid turbulence modification produced by these mechanisms, have to be accurately measured to be included on the empirical models used to design the energy transfer systems that are common in industry. Multiple experimental efforts have been directed towards this goal, and the open literature contains many examples of such works, but for brevity, we will refer to only a few.

A. Literature Review

1. Isothermal Two-Phase Flow

Isothermal air-water flow experiments were performed by Lance and Bataille [1] to understand the local void fraction (α) influence on the liquid phase turbulence. They used Laser Doppler Anemometry (LDA) and Hot Film Anemometry (HFA) measurements to study the turbulence of the liquid in a bubbly, grid-generated turbulent flow field. They found that the turbulent kinetic energy greatly increases with the void fraction. They described two regimes: the first one corresponds to low values of α, where hydrodynamic interactions between bubbles are negligible, and the second one to higher values, for which the bubbles transfer a greater amount of kinetic energy to

---

The journal model is *IEEE Transactions on Automatic Control*.

the liquid. The Reynolds stress tensor shows that the quasi-isotropy was not altered. Furthermore, their one-dimensional spectra analysis showed a large range of high frequencies associated with the wakes of the bubbles and the classical $^{-1}/_{5}$ power law is progressively replaced by a $^{-8}/_{3}$ dependence.

2. Non-Isothermal Single-Phase Experiments

Non-isothermal single-phase flow experiments were performed to elucidate the effect of density changes on the fluid turbulence within circular and square channels. Barrow [2] performed single-phase flow experiments in a rectangular channel with unequal heat fluxes in the channel walls. He analyzed the influence of uneven heating on friction and heat transfer coefficients and measured liquid velocity fields, but only for the unheated case. Roy et al. [3] pioneered on the research of turbulent liquid flow of refrigerant R-113 through heated and unheated annular channels. Using HFA they obtained mean axial velocity profiles and turbulence intensities for various Reynolds numbers and heat fluxes. They concluded that accurate velocity field measurements in turbulent liquid flow by constant temperature anemometry are difficult since generally only low sensor overheats can be used. Hasan et al. [4] obtained velocity and temperature fields of heated and unheated refrigerant R-113. Using HFA and a chromel-constantan microthermocouple, they presented radial profiles of velocity, turbulence intensities and Reynolds stresses, together with single-point correlations between turbulent velocity and temperature fluctuations. Wardana et al. [5] used Laser Doppler Velocimetry (LDV) and a resistance thermometer to study air velocity and temperature statistics in a strongly heated turbulent two-dimensional channel flow, with wall temperatures up to 700 ℃ and a fixed Reynolds number of 14000. They did not find significant changes by the wall heating in either temperature or velocity fields. However, they found a suppression of the turbulence intensities of

velocity fluctuations far from the heated wall. Velidandla et al. [6] used a two-component LDV and a micro-thermocouple to measure velocities and temperatures of refrigerant R-113. They found buoyancy effects on the time-mean velocity and turbulence fields, even at very low values of Gr/Re^2. Zarate et al. [7] developed velocity and temperature wall laws in a vertical concentric annular channel from measurements in turbulent liquid flow of refrigerant R-113, noting that when buoyancy forces influence becomes large, the velocity and temperature data do not follow the respective wall laws. Kang et al. [8] summarized experimental measurements on isothermal and heated turbulent up-flow of refrigerant R-113. They presented liquid turbulence statistics, radial turbulent heat flux distributions and Prandtl number estimations. Zarate et al. [9] presented numerical simulations to predict turbulent isothermal and heated up-flow of refrigerant R-113, providing comparisons with experimental results.

3. Subcooled Boiling Experiments

The firsts attempts known by the author to measure local fields of subcooled boiling parameters of the liquid phase was done by Roy et al. [10]. They measured turbulent velocity and temperature fields in the all-liquid region adjacent to a subcooled flow boiling layer. Significant changes in the turbulent structure of the all-liquid region were observed due to boiling. Improving their measurement techniques, Roy et al. [11] were able to measure liquid turbulence statistics of the liquid refrigerant R-113 even inside the boiling layer region adjacent to the heated wall. They found that the near-wall liquid velocity field was significantly different from that in single-phase liquid flow at a similar Reynolds number. Lee et al. [12] performed measurements of subcooled boiling flow of water in a vertical concentric annulus. Using a two-conductivity probe they measured the local void fraction and vapor velocity and using a Pitot tube they measured the liquid velocity. Situ et al. [13] measured the flow structure of subcooled

boiling flow in an annulus. They used a double-sensor conductivity probe method to measure local void fraction, interfacial area concentration and interfacial velocities. Using LDA Ramstorfer et al. [14] performed subcooled boiling flow experiments in a horizontal channel with one heated wall, to gain insight into the bubble laden near-wall velocity field. Contrary to the vertical channel experiments, they found that the streamwise velocity component was considerably reduced compared to the single-phase case, while the near-wall turbulence was increased due to the presence of the bubbles.

4. Numerical Simulations

Using the experimental information from the previous works, different two-phase flow models were developed and used to simulate convective subcooled boiling flow [15, 16, 17, 14] with some success. These models share the characteristics of being based on time-average analysis of information from point measurements probes. However, due to the complex nature of the turbulence found in subcooled boiling, this approach seems to be limited.

5. Visualization Techniques

Visualization techniques such as Particle Image Velocimetry (PIV) and Particle Tacking Velocimetry (PTV) can be used to overcome some of the limitations associated with point measurements techniques. PIV and PTV are non-intrusive and provides full-field quantitative and qualitative information of the flow under study with high spatial and temporal resolution. The common measuring principle behind these methods is that instantaneous fluid velocities can be evaluated by recording the position of images produced by small tracers suspended in the fluid, at successive time instants. The underlying assumption is that these tracers closely follow the fluid motion with

minimal lag. This assumption holds true for a wide variety of flows of interest provided that the tracers are small enough and/or their density approaches that of the fluid. Besides their common goal, an important difference is that in PIV, the concentration of tracers is rather high and the measurement of the "local" fluid velocity results from an average over many tracers contained in a measurement volume. This is in contrast with PTV, where the velocity is determined at random locations using the images produced by a single tracer. Although both techniques can be applied on the analysis of two phase flows, PTV is preferred, due to its ability to differentiate between the gas and liquid phases and subsequently deliver simultaneous velocity fields associated with each phase.

6. Two-Phase Flow Experiments with Visualization Techniques

Using PTV adiabatic two-phase flow experiments had been carried out [18, 19, 20] to investigate the influence of void fraction on liquid turbulence parameters. These experimental studies represent a rich description of phenomenological events important for the modeling of two-phase flows. However, there appears to be a scarcity of subcooled boiling experimental studies that can capture instantaneous whole-field measurements with a fast time response.

7. This Work

In this work, time resolved PTV experiments are performed to obtain liquid flow measurements in turbulent subcooled boiling flow of refrigerant HFE-301 (3M, Novec-7000) [21] through a rectangular channel. This work is an attempt to enrich the database already collected on turbulent subcooled boiling flow and to provide a mean for validation and improvement of two-phase flow numerical models.

CHAPTER II

EXPERIMENTAL APPROACH

A. Experimental Facility

The experimental facility was designed for the visualization of subcooled boiling flow of refrigerant HFE-301 at low system pressures. The facility consists of a hydraulic loop and a visualization system. Requirements such as temperature, pressure and fluid compatibility were considered in the hydraulic loop design, and dynamic arrangement to facilitate optical access was considered on the visualization system. More details are given in the following sections.

1. Hydraulic Loop

The hydraulic loop facility consisted of an external loop and a test section. The external loop and test section were designed to withstand temperatures in excess of 200 ℃ and pressures up to 100 psi. The external loop consisted of piping, fittings, valves, a reservoir tank, circulation heater, filters, a heat exchanger, and a pump. All the component materials were chosen to be compatible with the Novec 3M 7000 fluid. Nylon tubing with brass compression fittings were used in the loop to meet these conditions. Although the Novec fluids have a low toxicity, a closed loop was chosen to reduce the exposure and evaporation of the fluid. The loop was constructed in a modular fashion with the test section isolated from the rest of the loop. This was done to reduce vibrations in the test section from the pump and to allow for the test section to easily be removed for assembly and repair. The flow loop is attached to a board that can be leveled for precise measurements of the test section.

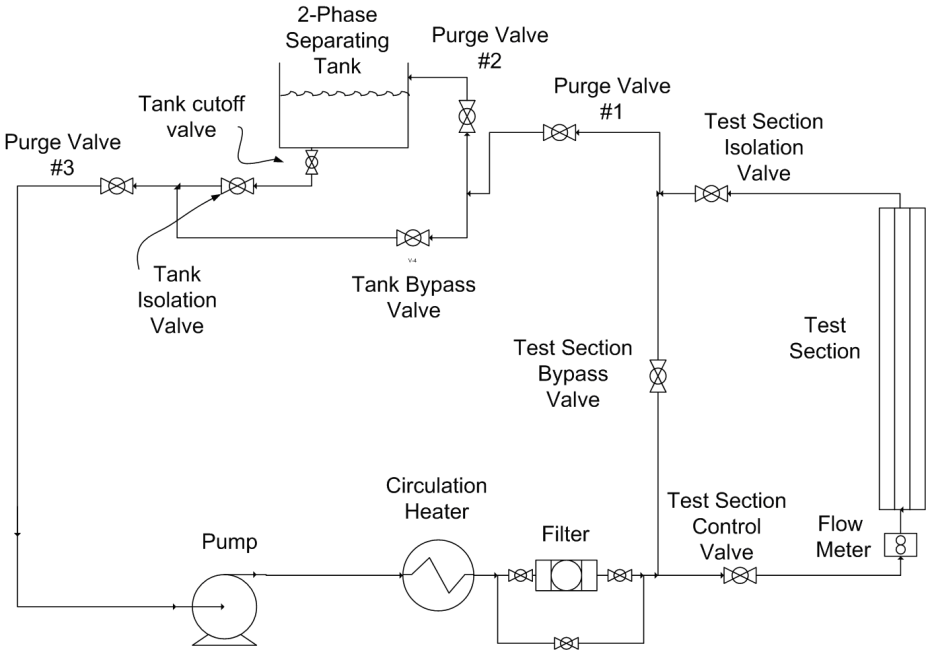

Fig. 1. External flow loop schematic.

Fig. 1 shows the external loop that has been designed and constructed for the experiment. Here, a two-phase separating tank is used to fill the loop with the working fluid. A start-up and purging procedure is used to purge the loop of any air. First purge valves #1 and #3 are closed while the tank cutoff, tank isolation, tank bypass and #2 purge valves are opened. The tank is filled with fluid and the lines between purge valve #1 and #3 are filled. Next the tank bypass valve is closed and purge valve #3 is open. The pump is started and all remaining valves are opened and the fluid is pumped through the system. The remaining air is eliminated from the system when it enters the two-phase separating tank. Once all the air has been removed, the #2 purge and tank isolation valves are shut and the tank bypass is opened and a closed loop is achieved. The fluid is then filtered through for 10-30 minutes to eliminate any

large seeds in the flow or any contamination. The filter is then bypassed to reduce the pressure drop in the system.

The temperature of the fluid to the test section is controlled by means of a Watlow circulation heater. This heater is managed by an internal PID temperature controller, capable of a fast response to temperature changes. The mass flow rate to the test section was measured with a variable-area flow meter and controlled by adjusting the test section bypass and control valves.

The test section is a rectangular channel made of transparent polycarbonate, with 530 mm length and a cross-sectional area of 8.7×7.6 mm^2. Energy for boiling is provided by a Kapton thin heater with a length and width of 175 mm and 7 mm, respectively, and a maximum working temperature of 200℃. The heater is attached to the lateral interior face of the channel (see Fig. 2). The electric current to the heater is provided and adjusted by a DC power supply, from which a maximum wall heat flux of 64 kW/m^2 was obtained. To reduce heat losses to the ambient, the external face of the channel was insulated with 10 mm of balsa wood. With this configuration an unheated length of 320 mm is achieved. To measure the heater wall temperature, six J-type thermocouples were attached to the external face of the heater. The thermocouples were positioned in a vertical arrangement along the heater wall with a space of 25.4 mm in between them. Test section fluid inlet (T_{in}) and outlet (T_{out}) temperatures were also measured by two J-Type thermocouples. Fig. 2 shows the schematics and dimensions of the test section.

2. Visualization System

The visualization system consisted of particles flow tracers, a high-speed high-resolution camera, a high-speed high-power laser, a continuous halogen lamp, mirrors, translational stages, and lenses. The flow tracers are highly reflective silver coated particles

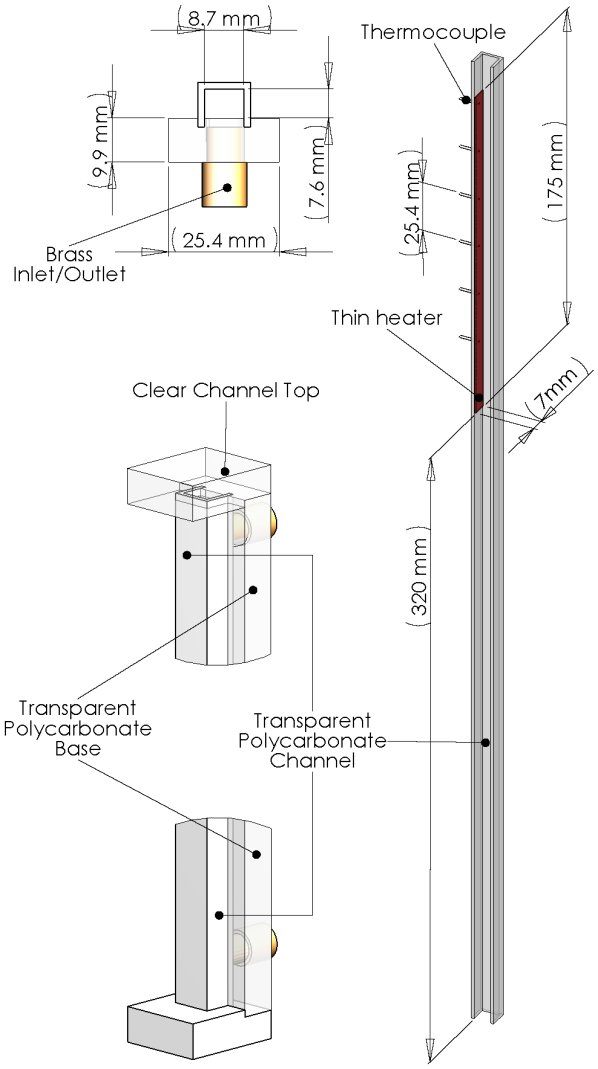

Fig. 2. Test section schematics and dimensions.

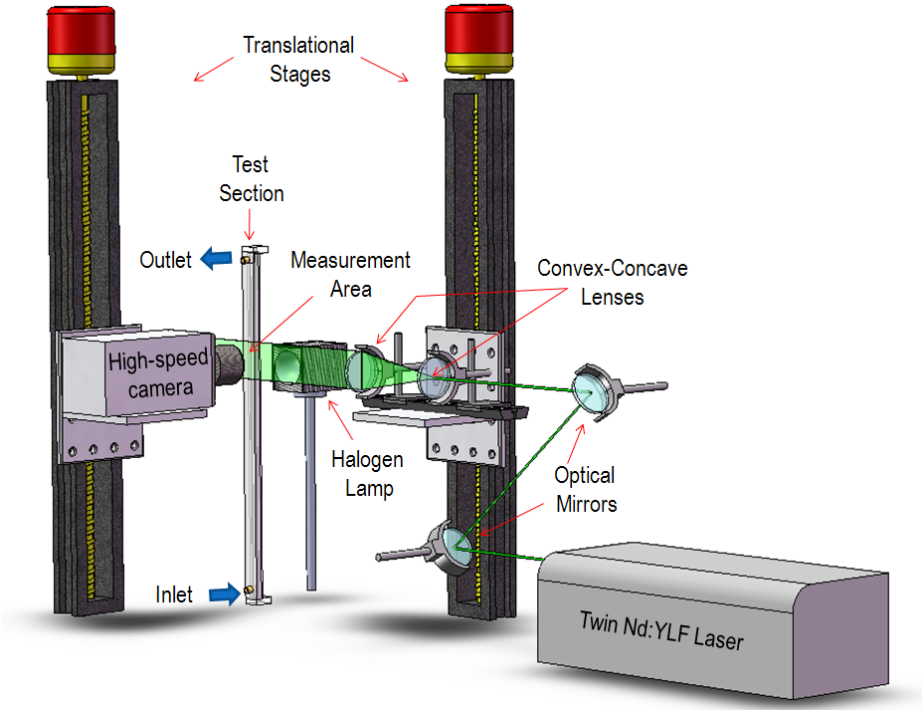

Fig. 3. Visualization system schematics.

with a density range of 1.39 to 1.41 kg/m^3, with an average particle diameter of 40 µm. The high-speed camera has a maximum frame rate of 7000 fps at a resolution of 800×600 pixels, with a maximum bit depth of 12 bits. The illumination was provided by a Pegasus laser dual lamp with a maximum power of 27 mJ/pulse and a maximum pulse rate of 20000 pulse/s. Two optical mirrors and two concave-convex lenses are used to convert the small circular beam from the laser, into a thin sheet of light. The laser light sheet is positioned on the measurement area region, parallel to the camera focal area. The camera, mirrors and lenses are mounted on translational stages to have the capability of changing the measuring region along the test section. Fig. 3 shows the schematics of the visualization system.

CHAPTER III

PTV SYSTEM AND ACCURACY

A. PTV Algorithm Description

To measure the liquid velocity on the subcooled boiling flow experiments, a home-developed PTV algorithm is used. This algorithm has been applied successfully on previous two-phase flow works [18, 19, 20]. The original algorithm was developed by Cannan and Hassan [22], and has been improved over the years. A simplified description of the PTV algorithm follows: 1) particle detection, 2) particle centroid location estimation and 3) particle matching in between consecutive frames (particle tracking). In this section, the components of the PTV algorithm that are new or relevant for the present study are described below. A more detailed description of the PTV processing is given elsewhere by Estrada-Perez [23].

1. Particle Detection

The particle detection procedure is specially important in any multi-phase flow experiment, where accurate identification and discrimination in between phases is required. This procedure provides important particle parameters such as size, shape and interface interactions. In this study particle mask correlation method [24] is used to this end. This technique is an image template matching routine, where the selected template is an ideal particle image generated from the following equation

$$\begin{aligned} I(x,y) &= I_0 \exp\left[-\frac{1}{2r_0^2}\left(\frac{(x-x_0)^2}{a^2}\right.\right. \\ &\quad \left.\left.+\frac{(x-x_0)(y-y_0)}{c^2}+\frac{(y-y_0)^2}{b^2}\right)\right] \end{aligned} \tag{3.1}$$

This equation will generate a Gaussian representation of an ideal particle where I(x,y) is the gray scale intensity on the (x, y) position, (x_o, y_o) is the particle centroid location, I_o is the maximum intensity, a, b, and c are shape modifier parameters, and r_o is the particle radius. The image template selection will depend on the object of interest, for example, selecting a small value for r_o (particle size) will in turn provide a means of discerning in between small and large objects.

2. Particle Centroid

Once a particle (or object) is identified, its centroid is estimated to sub-pixel accuracy. In this study three different centroid estimation techniques are available: three point Gaussian interpolation (3PGI) [25], two dimensional Gaussian regression (2DGR) [26], and center of mass technique (CMT). 3PGI and 2DGR performance and accuracy are similar, both are well suited for small (radius $<$ 10 pixels) Gaussian shaped objects. The CMT is better suited for larger objects (radius $>$ 10 pixels) with no shape restriction. For example, in a two phase flow PTV experiment, CMT will be ideal for bubbles centroid location, and either 3PGI and 2DGR are well suited to estimate the liquid tracer particles centroids. Although 3PGI technique is the most commonly used among researchers due to its simplicity, in this work, 2DGR is preferred since it relies on more information (9 points are used in the regression rather than 6) to estimate the centroids.

3. Particle Tracking

The particle tracking algorithm used in this study, is based on direct spatial correlation. This is a straightforward manner to compute the cross-correlation. It computes a correlation coefficient between two sub-images that are inside a pair of single-exposed

PTV pictures. The correlation coefficient between the sub-images I_A and I_B with $a \times b$ dimensions is computed using

$$\begin{aligned} C_{I_A I_B}(x_o, y_o) = & \sum_{i=1}^{a} \sum_{j=1}^{b} \left[I_A(i,j) - \bar{I}_A \right] \left[I_B(i,j) - \bar{I}_B \right] \\ & \times \left(\sum_{i=1}^{a} \sum_{j=1}^{b} \left[I_A(i,j) - \bar{I}_A \right] \right)^{-1/2} \\ & \times \left(\sum_{i=1}^{a} \sum_{j=1}^{b} \left[I_B(i,j) - \bar{I}_B \right] \right)^{-1/2} \end{aligned} \tag{3.2}$$

where $\bar{I}_A$ and $\bar{I}_B$ are the average intensities of sub-images A and B respectively. In this study, the two sub-images are particle images in consecutive frames. Assuming two experimental pictures, A and B acquired at two different times $t = t_o$ and $t = t_o + \Delta t$ respectively, the correlation coefficient will determine which particle in picture B is the best match of a particle on picture A. Since particles location is estimated to sub-pixel accuracy, and the interval between pictures is known, an accurate particle velocity estimation is available.

B. PTV Algorithm Accuracy

Using sets of artificial and experimental images, the PTV algorithm error sensitivity analysis was developed by Estrada-Perez [23]. Some of the relevant results are summarized next.

1. Particle Detection and Centroid Estimation Errors

Fig. 4(a) shows the centroid estimation error as a function of particle size. For the actual boiling experiments, the average particle image radius was about 3 pixels, where the algorithm RMS error for particle position is below 0.01. This particle image size was obtained with a trade-off between camera magnification, resolution and particle dimensions. Since particle dimensions and camera resolution are fixed (30 to 40 µm and 800×600), the required magnification provided a visualization area of 9.87×7.40

mm^2 with 81.03 pixels/mm. Fig. 4(b) (where optimal particle dimensions were considered) presents centroid estimation error as a function of particle image density. As expected, increasing particle image density will increase the centroid estimation error. In overcrowded pictures, particle images are closer or even overlapped, making discerning individual particle detection more difficult. In the boiling experiments, an average of 3000 particles in a 800×600 image (equivalent to 1562 particle in a 500×500 image) was obtained, corresponding to an RMS value of 0.02. Fig. 4(c) shows the effectiveness of the particle detection algorithm (for optimal particle image dimensions). Both 2DGR and 3PGI have acceptable performances even for high particle image densities, these techniques accurately detect and estimate the centroid of overlapped particle images. CGT lacks of this capability, therefore, strongly overlapped particles will be considered as a single particle, affecting both efficiency and accuracy. For the boiling experiments 2DGR was used with an experimental particle image density of 1562 particles. This provides an experimental particle image detection efficiency of about 98%.

2. Velocity Estimation Accuracy

The velocity accuracy was tested with home-made artificial images and with the international standard PIV challenge artificial images [27]. From this analysis, a maximum velocity estimation error for the current experimental image conditions was estimated to be less than 0.1 pixels (1.2 μm).

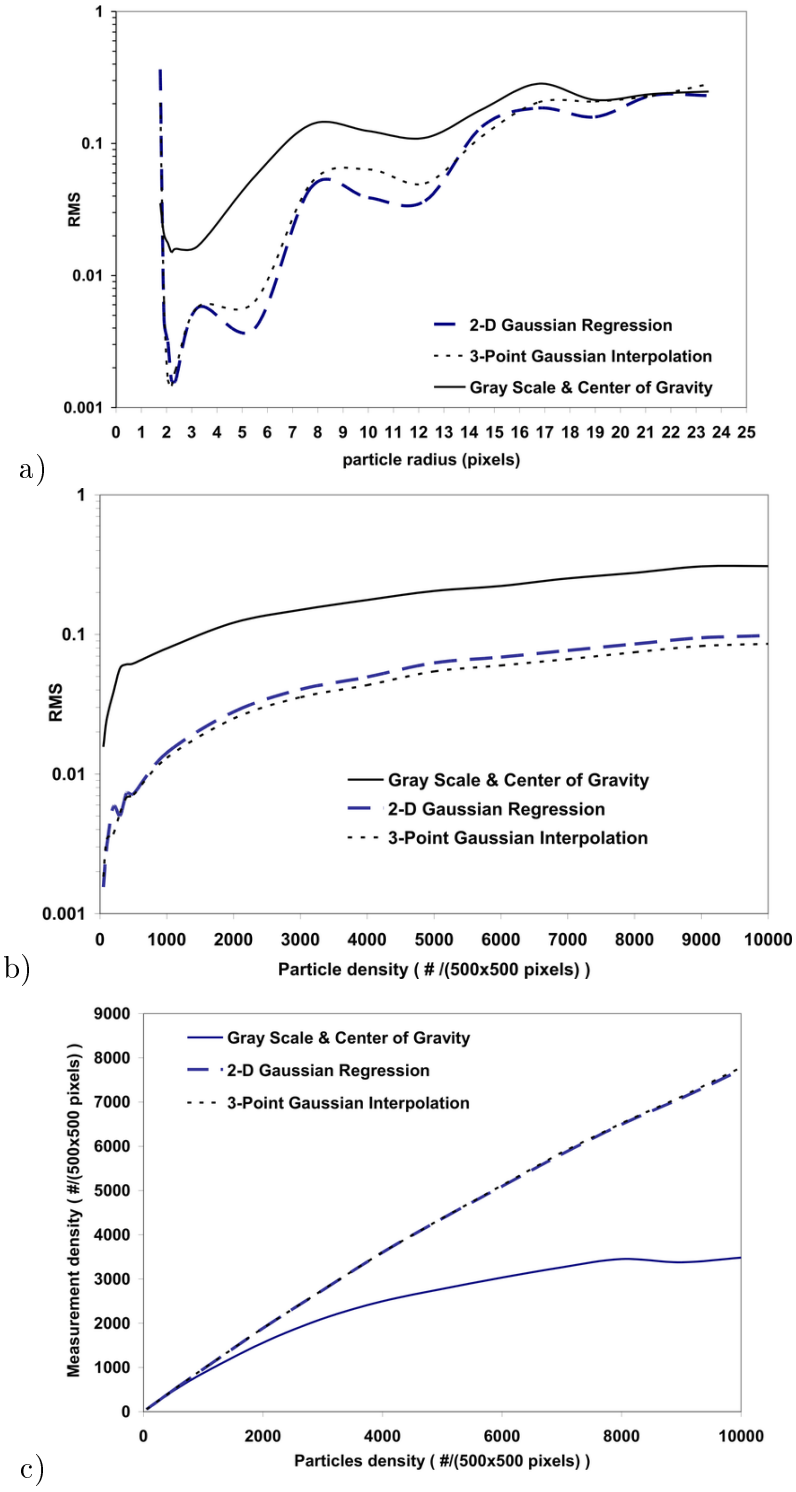

Fig. 4. Centroid estimation error sensitivity analysis.

CHAPTER IV

EXPERIMENTAL UNCERTAINTIES

In this section a summary of experimental uncertainties is presented, details of each uncertainty calculation are given on Appendix A.

A variable area flow-meter model F-450 from Blue-White industries, was used to measure the volumetric flow rate through the test section. The full-scale accuracy accounts for ±5%. Additional corrections were needed since water was used for the flow-meter factory calibration. The correction formula for a working fluid with density of 1400 kg/m^3 is $\dot{Q}_C = \dot{Q}_M \times 0.6842$, where $\dot{Q}_C$ and $\dot{Q}_M$ are the corrected and the measured volumetric flow rates.

Temperature measurements were performed with J-type Omega thermocouples with ±2.5 ℃ tolerance between -40 ℃ and 375 ℃. To measure outside heater wall temperature, six thermocouples were attached along the outside heater wall (see Fig. 2). Direct measurements of inside wall temperature were not performed to avoid liquid flow disturbances in the near-wall region. To estimate inside wall temperature from the outside wall temperature, a calibration curve was obtained by means of experiments. For the calibration experiments, two thermocouples were used, one measuring the outside heater wall temperature (T_{out}) and the other measuring the inside wall temperature (T_{ins}), both thermocouples positioned at the same height. Different flow rates and heat fluxes were considered. For the range of experimental conditions of interest, a maximum wall temperature ratio was found to be T_{out}/T_{ins} = 1.3.

The heater power was calculated as the product of the current and the voltage difference across the heater. The D.C. power supply (Mastech D.C. HY3020MR)

voltage and current reading accuracy accounted for ±1 % and ±2 % respectively, from which a heater power measurement accuracy of ±2.23 % was calculated with the error analysis suggested by Kline and McClintock [28].

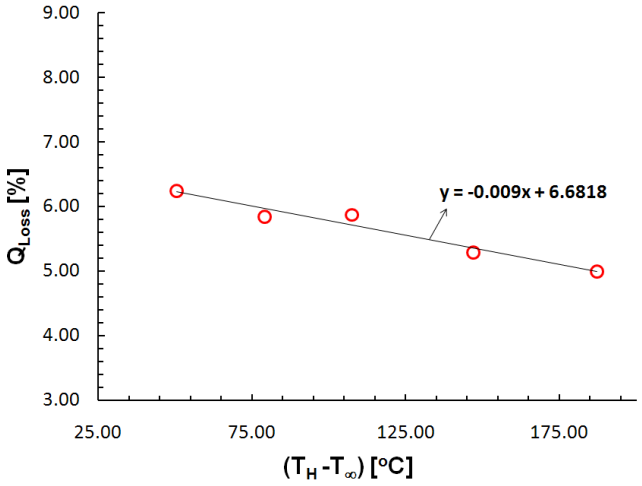

Fig. 5. Percentage of heat loss as a function of liquid temperature difference (T_H - T_∞).

The heat losses from the test section to the ambient were calculated with a heat balance from experimental data obtained under no-liquid, no-flow conditions, with power ranges from 5.01 to 13.72 W. Fig. 5 shows the percentage of heat loss (Q_{LOSS}%) as a function of temperature difference between wall heater temperature (T_H) and ambient temperature (T_∞). The maximum temperature difference ($T_H - T_\infty$) in the boiling flow experiments is about 65 ℃ giving an average heat loss of about 6%.

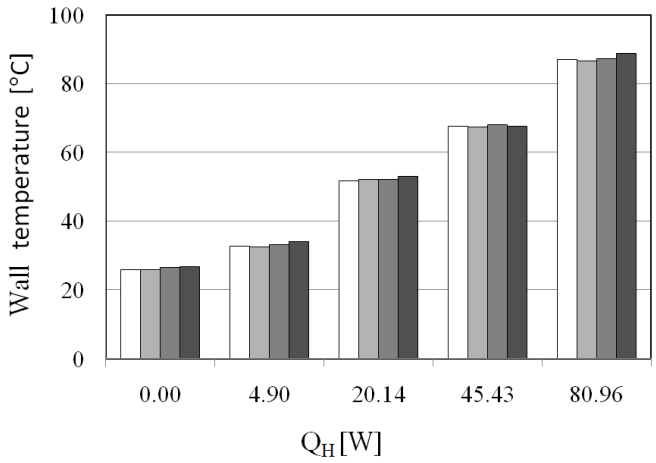

Fig. 6. Wall temperature comparison for case a) reference □, b) PTV particles ■, c) halogen illumination ■, d) laser illumination ■

A. Influence of Visualization Devices on Temperature Measurements

The fluid turbulence modification due to changes of wall heat flux can not be correctly assessed if there is not an estimate of the additional energy provided by the flow visualization devices, therefore convective boiling experiments with Re = 9929.82 and heater power values (Q_H) of 0.0, 4.98, 15.13, 45.42, and 80.56 W were performed considering four different cases: a) reference (no visualization devices), b) fluid with particle tracers, c) fluid with halogen light illumination and particle tracers, and d) fluid with laser light illumination and particle tracers. In these experiments three hours were used as a steady state waiting time, after which, temperature measurements were acquired for 10 seconds at a rate of 2000 Hz. The heater wall temperature at different heights, the channel inlet and outlet fluid temperatures and the ambient air temperature were measured for each case. Fig. 6 shows the heater average wall temperature ($\bar{T}_{wall}$) for the different cases. There are not noticeable differences on

$\bar{T}_{wall}$ within the cases, being the largest difference of 2.18 ℃ found between the reference case and the case with laser illumination.

Fig. 7 shows the effects of illumination devices on the difference between inlet and outlet liquid temperatures ($\Delta T_f = T_{out} - T_{in}$) for different heater powers. The effect of the illumination devices on ΔT_f is also negligible, having a maximum absolute difference value of 0.15 ℃ (lower than the temperature measurement uncertainty). It can be concluded that the effect of the illumination devices on the overall heat transfer of the system is negligible small and within the values of the temperature uncertainties. Further investigations are needed to determine the local effects induced by the illumination devices.

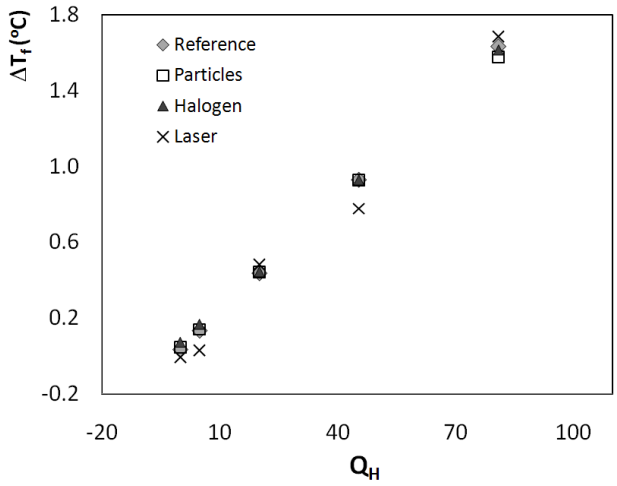

Fig. 7. Differences between channel outlet and inlet fluid temperatures measured for each different illumination case for different heater powers.

B. Other Uncertainties

On PTV measurements, a source of error is induced by gravitational forces if flow tracers density differ largely from that of the liquid. An indication whether gravitational forces becomes important, can be obtained from Stokes drag law [29], from which the gravitational induced velocity U_g is given by

$$U_g = d_p^2 \frac{(\rho_p - \rho)}{18\mu} g \tag{4.1}$$

where d_p and ρ_p are diameter and density of the particles, ρ and μ are the density and dynamic viscosity of the liquid, and g is the gravitational acceleration. In the subcooled boiling experiments the liquid density gradient induced a maximum gravitational velocity of $U_g = 2.4$ μm/s, therefore the influence of liquid density changes on velocity estimation can be neglected.

Further investigation of the PTV velocity measurement accuracy was performed by comparing PTV measurements with the flow meter readings. The average velocity obtained with PTV was 10% larger than the measured by the flow meter. The reason of this discrepancy is attributed to the fact that PTV measurements were acquired in the center plane of the channel, where the maximum velocity is located. If more planes were considered for the PTV measurements, then this discrepancy should decrease.

Sampling number is another factor that influences the velocity measurement accuracy. In this work, the sampling number corresponds to the number of PTV velocity fields (or number of PTV image pairs) used to estimate the liquid average velocities. The sampling number influence on the velocity measurement uncertainty is determined experimentally as shown in Fig. 8, where $\Delta\bar{X}(\bar{X} : \bar{U}, \bar{V})$: is defined as

$$\Delta\bar{X} = \frac{\bar{X} - \bar{X}_m}{\bar{X}_m} \tag{4.2}$$

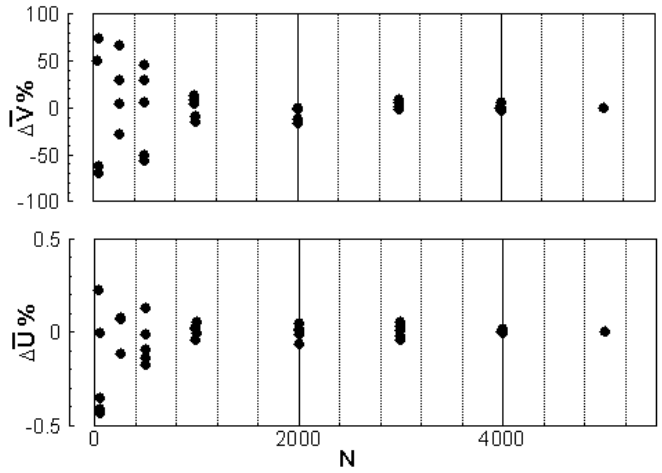

Fig. 8. Sampling number effect on velocity measurements uncertainty.

in this case $\bar{X}$ is the average value calculated using N velocity fields and $\bar{X}_m$ is the mean value of $\bar{X}$. As shown in Fig. 8 the average normal velocity uncertainty is less than 5% after a sampling number $N = 3000$, while the average axial velocity uncertainty is less than 5% after a sampling number $N = 250$, therefore for the boiling experiments, a sampling number of 5000 is used to yield reasonable statistical estimations of the flow average velocities.

CHAPTER V

RESULTS

A. Flow Characterization Experiments

To characterize the flow, liquid velocity measurements were performed using PTV at different positions along the channel. The visualization facility allowed changing with minimum effort the measurement region along the length of the channel (see Fig. 3). Three different measurement regions were selected, the distances from the measurement region location to the channel inlet are shown in Table I.

Table I. Test section measurement names and positions

Name	Distance from the inlet
P56	455 mm
P23	365 mm
N10	275 mm

For each measurement region, 3000 pictures were acquired using the high speed camera. The camera was synchronized with the high energy laser that provided a 1 mm thick sheet of light for illumination. The camera frame rate was 2500 frames/s with an exposure time of 2 µs; each image consisted of 504×800 pixels with a spatial resolution of 20.1 µm/pixel, with this configuration, the whole channel width was visible inside the measurement region. A Reynolds number of $\mathrm{Re} = 9929$ was consid-

ered in this experiment, and a constant inlet temperature of 25.5 ℃ was maintained. Fig. 9 shows the mean axial velocity $\bar{U}$ and mean axial turbulence intensity u' for the different measurement regions, both normalized by the mean centerline axial velocity ($\bar{U}_c$). The distance from the wall is normalized by the channel half-height (h).

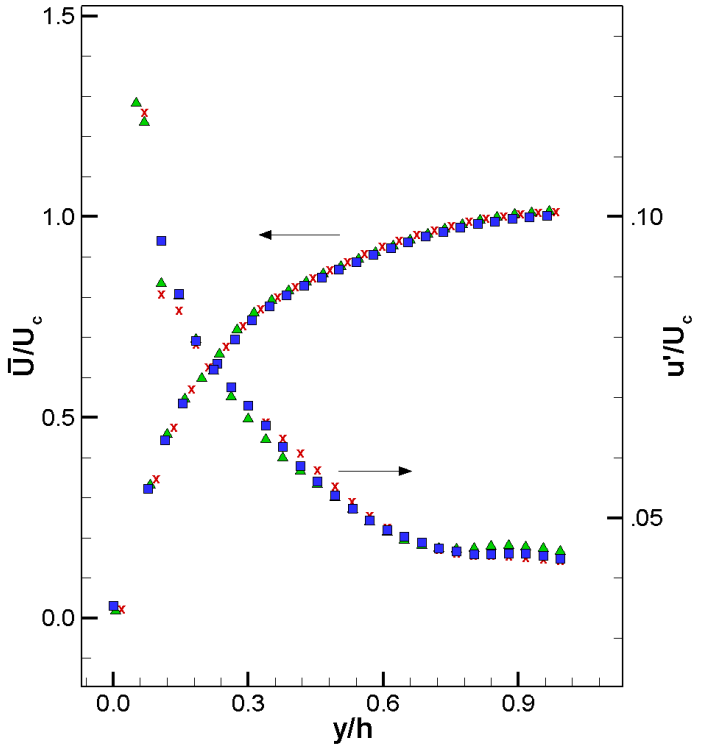

Fig. 9. Mean axial velocity $\bar{U}$ and axial turbulence intensities u' profiles at position 455 mm ×, 365 mm ■, 275 mm ▲, from the channel inlet

The turbulence intensity profiles showed small discrepancies between the measurement regions, these differences may be the result of having a small ratio of channel width and height ($w/H \approx 1$), which means that the flow is not entirely two-dimensional. This channel design was chosen to simulate the small ratios of w/H

typically found in the coolant flow channels of boiling water nuclear reactors (BWR). Ideally, the mean normal velocity $\bar{V}$ should be zero, however in this experiments nonzero values of this velocity were measured, but were only about 0.7% of the mean axial velocity component in the flow core region. The normal velocity profiles are not shown for these experiments. Measurement region P56 (see Table I) was selected as a suitable measurement area for the boiling experiments, because at this position fully developed flow statistical characteristics were found. Also because there are two adjacent thermocouples at this location, that provide good local estimates of average heater wall temperature. Flow development from lower measurement areas is known and can be used as inlet boundary conditions for computer simulations.

B. PTV Subcooled Boiling Flow Experiments

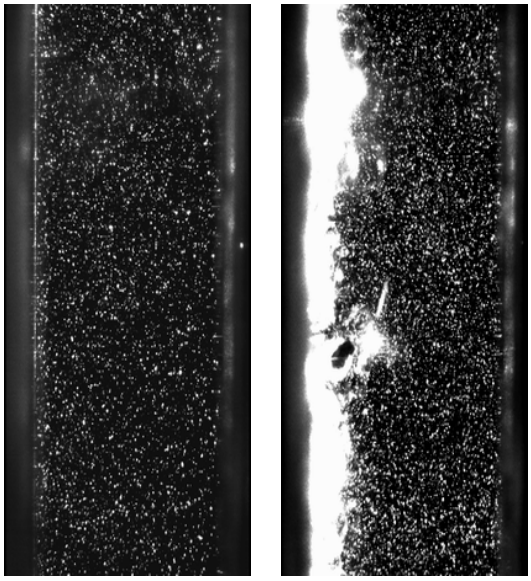

(a) (b)

Fig. 10. PTV experimental images (a) unheated single-phase flow (b) boiling flow with $q'' = 56.9$ kW/m^2.

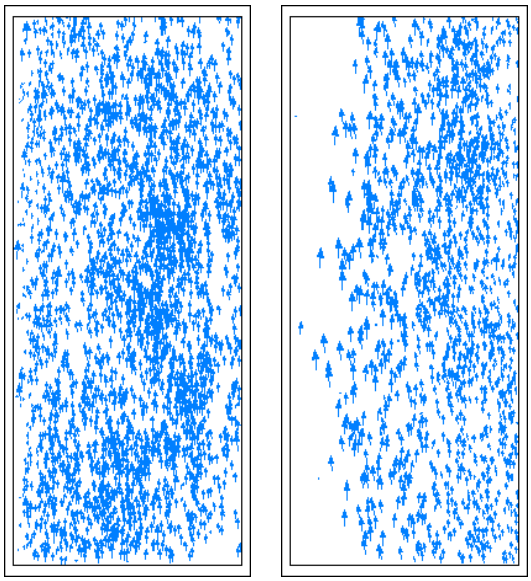

(a) (b)

Fig. 11. Velocity fields obtained from experimental images for (a) unheated single-phase flow, (b) boiling flow with $q'' = 56.9$ kW/m^2.

The measurement area selected was located at 455 mm (position P56) from the channel inlet. At this position PTV experiments to obtain liquid velocity measurements were performed with a camera frame rate of 3500 frames/s, and an exposure time of 2 μs. Each acquired image consisted of 600×800 pixel with a spatial resolution of 12.3 μm/pixel. Three different Reynolds numbers were considered: 3309, 9929 and 16549, for each Reynolds about 13 different heat fluxes (q'') were used, ranging from 0.0 to 64.0 kW/m^2. For all cases a constant inlet temperature of 25.5 ℃ was maintained and the heater wall average temperature and fluid outlet temperature were also measured. Fig. 10 shows the PTV experimental images for a Re = 9929. Fig. 10(a) presents the unheated single-phase flow images, where the flow seedings are easily identified from the black background. The heated single-phase experimental images are similar and are not shown for brevity. Fig. 10(b) presents the boiling flow

images at a heated condition of $q'' = 56.9$ kW/m^2. A bubble layer is shown on the left side of the channel where boiling is occurring. From these images, bubbles can be discriminated from the flow seedings due to differences in size, gray scale value and shape. Fig. 11 shows instantaneous velocity fields obtained from experimental images at Re = 9929. Fig. 11(a) shows the instantaneous velocity field from the unheated single-phase flow experiments. Similarly, Fig. 11(b) shows the instantaneous velocity field obtained from the boiling flow experiment. Vector gaps are found at positions fully occupied by bubbles, confirming that only the liquid velocity is being obtained, it is also noticeable that the vector magnitude difference in between the two cases is larger in regions close to the heated wall (left part of the channel).

1. Heat Flux Influence on the Liquid Phase Turbulence

Wall heating brought significant changes in the velocity distribution profiles. Some of these changes are general trends observed also by other researchers [10, 30, 12], and are summarized next: First, the mean liquid axial velocity in regions close to the heated wall increased accompanied with a decrease in the axial velocity for regions far from the heated wall. Second, there is a marked shift of the maximum liquid axial velocity location toward the wall. These trends are observed on Fig. 12. Fig. 12 (a) shows the profiles of mean liquid axial velocity $\bar{U}$ for Re = 3309 with wall heat fluxes ranging from 0 to 64 kW/m^2. It is observed that for wall heat fluxes ranging from 3.9 to 9.0 kW/m^2 the increase of velocity close to the wall shifted the maximum towards a common position located at about y = 2.5 mm.

These heat fluxes shared a common maximum velocity magnitude of about 0.2 m/s. Further increase in the heat flux forced the maximum velocity magnitude to increase and to shift closer to the wall (y $\sim$ 0.5mm). This behavior is observed up to a heat flux of 42.3 kW/m^2. The velocity profiles for these heat fluxes intersected at

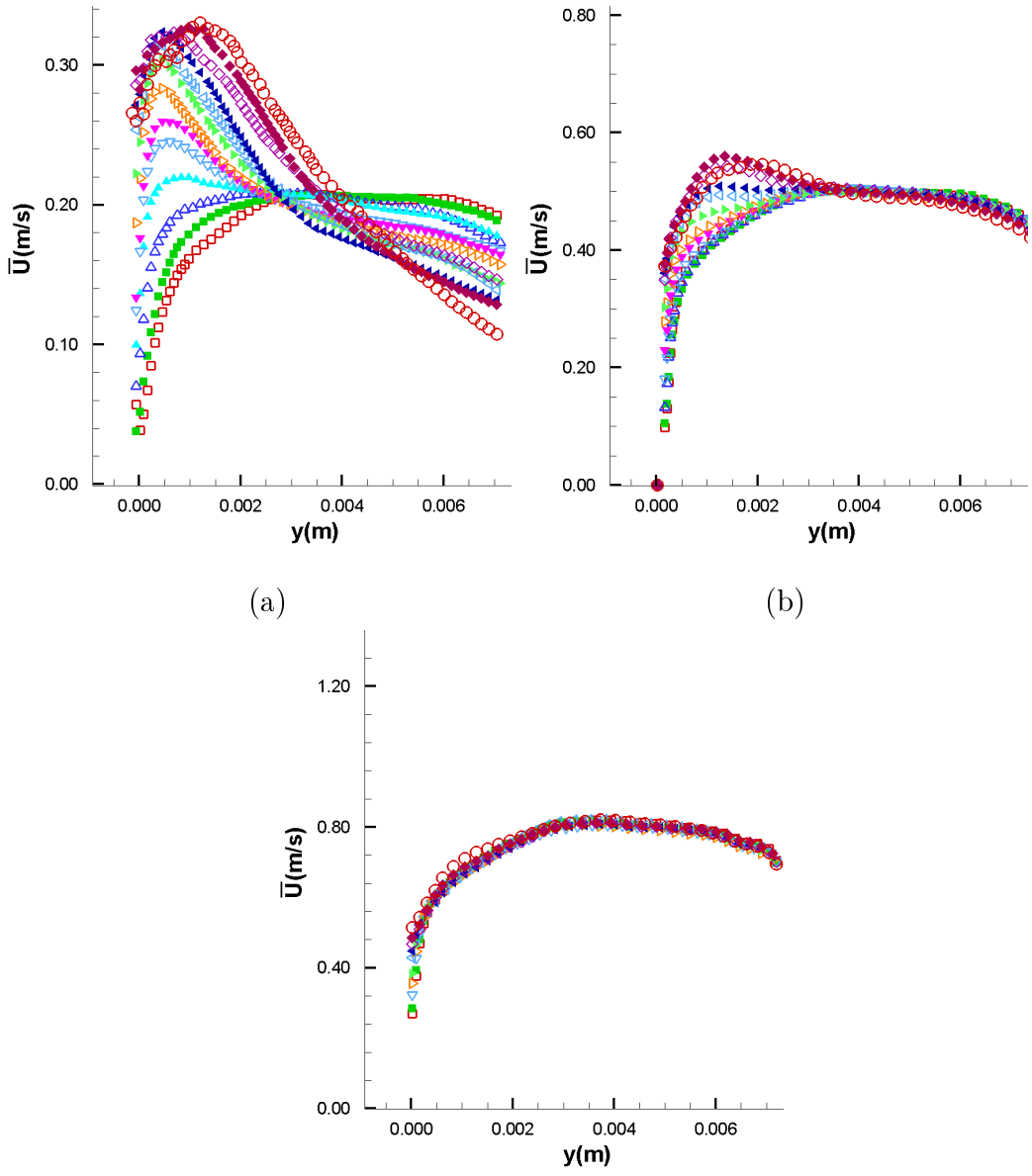

Fig. 12. Mean axial liquid velocity profile for (a) Re = 3309, (b) Re = 9926, (c) Re = 16549. with $q'' = 0.0$ □, 3.9 ■, 9.0 △, 12.2 ▲, 16.0 ▽, 18.3 ▼, 20.3 ▷, 22.3 ▶, 35.9 ◁, 42.3 ◀, 48.7 ◊, 56.6 ⧫, 64.0 ◯ [kW/m^2]

a common position (y = 2.5 mm). The general trends previously mentioned changed for the highest heat flux cases (from 48.7 to 64.0 kW/m^2). For these cases new trends were found: First, the maximum liquid axial velocity reaches a "terminal" maximum velocity of about 0.34 m/s, and second, the maximum liquid axial velocity starts shifting away from the wall towards the center of the channel. Furthermore, the common intersecting point found for the lower heat fluxes (y = 2.5 mm) is not longer present for the higher heat flux cases. Instead a shifting of this point towards the center of the channel is observed. The "new" trends were also observed for the medium Reynolds number case (Re = 9929) shown in Fig. 12(b).

With this Reynolds number, the influence of wall heat flux over the axial velocity follows the same general trends as the observed for the lower Reynolds case (Re = 3309), however the increase of axial liquid velocity due to the increase of wall heat flux is dampened, and the velocity reduction effect for regions far from the wall is still present, but with less magnitude. The unheated single-phase profile, together with those of low heat flux (0 to 16.0 kW/m^2), showed no significant differences in the velocity profiles, only small discrepancies for points close to the heater wall are noted. For medium heat fluxes (18.3 to 35.9 kW/m^2), there is an increase of the axial velocity, persistent from y = 0 to about y = 3.5 mm. The "new" trends started to be observed on the heat flux range from 42.2 to 56.3 kW/m^2, where the increase in axial velocity follows the same behavior of the medium heat flux cases; however, the maximum velocity location is shifted away from the wall towards the center of the channel. When reaching the heat flux of 64.0 kW/m^2, the maximum velocity location is also shifted to the right followed by a reduction of velocity magnitude for points close to the wall. This "new" trend is similar to the one found for the higher heat flux cases of the Re = 3309 experiment, with the difference that the "terminal" maximum velocity is now about 0.54 m/s. Fig. 12(c) shows the profiles of mean liquid

axial velocity $\bar{U}$ for Re = 16549 with wall heat flux ranging from 0 to 64 kW/m^2. It is clear that at this Reynolds, the heat flux influence seemed to be minimal. The increase of velocity for regions close to the wall as a function of wall heating is small and velocity reduction for regions far from the wall is not noticeable. Small changes start appearing only up to a wall heat flux of 56.6 kW/m^2, where a small increase of velocity is observed for points in the region from y = 1.0 to about 2.5 mm.

2. Liquid Turbulence Statistics

Since most of the changes in the liquid behavior due to wall heating are observed close to the heater wall, it is common to use wall coordinates. In the wall coordinate system, a characteristic velocity is needed to obtain non-dimensional variables. This characteristic velocity was chosen to be the friction velocity ($u^* = [\tau_w/\rho]^{1/2}$). The friction velocity can be estimated by plotting the dimensional total stress profile and taking a best fit of the near-wall total stress to determine τ_w. It should be noted here, that the non-dimensionality is performed with single-phase unheated wall values. i.e., using the friction velocity for the single-phase unheated case. Following the previous procedure the friction velocities obtained for Re = 3309, 9929, and 16549 were respectively u^* = 0.012, 0.027, and 0.040 m/s. The overall influence of wall heating over the axial velocity was explained in the previous section, while some remarks concerning the applicability of the wall law are discussed next. All results presented in this section are normalized by the corresponding single-phase unheated friction velocity for each Reynolds number. Fig. 13 shows the axial non-dimensional velocity profile versus the non-dimensional distance from the wall ($y^+ = yu^*/\nu$) at various values of wall heating for Re = 3309, 9929, and 16549. From Fig. 13(a), it is clear the significant influence of heat flux for the low Reynolds number case. Only the unheated single-phase flow case ($q'' = 0$) has a fairly good approximation to the

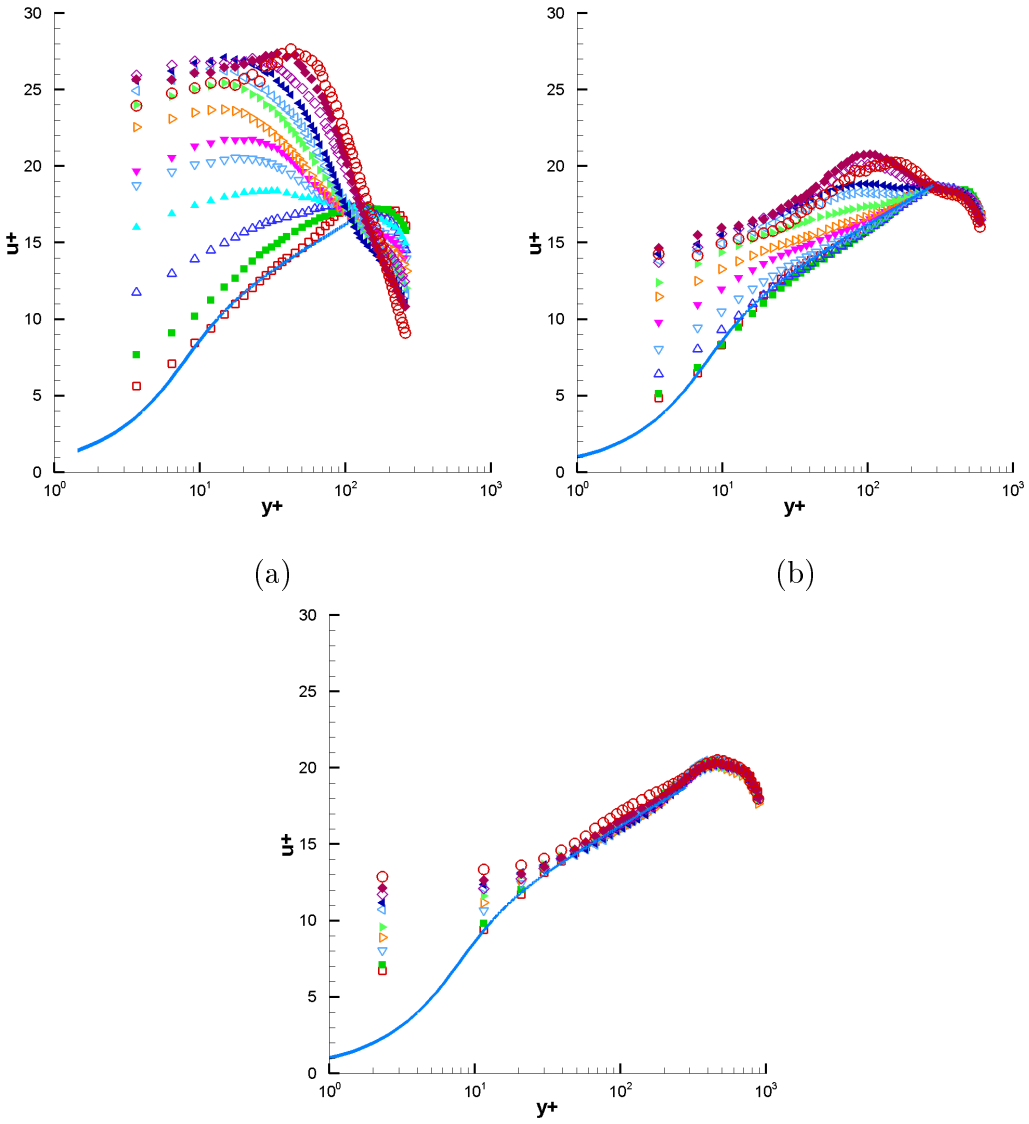

Fig. 13. Mean axial liquid velocity profile normalized with single-phase flow friction velocity for (a) Re = 3309, $u^* = 0.012$ m/s, (b) Re = 9926, $u^* = 0.027$ m/s, (c) Re = 16549, $u^* = 0.040$ m/s, with $q'' = 3.9$ ■, 9.0 △, 12.2 ▲, 16.0 ▽, 18.3 ▼, 20.3 ▷, 22.3 ▶, 35.9 ◁, 42.3 ◀, 48.7 ◊, 56.6 ♦, 64.0 ◯ [kW/m^2]

law of the wall. Fig. 13(b) shows that the single-phase profile, together with those of low heat flux (0 to 9 kW/m^2), showed no significant differences from the law of the wall, and only small discrepancies for points close to the wall heater were noted. For higher heat fluxes these discrepancies increased. For the highest Reynolds number, (Fig.13(c)) most of the heat flux cases considered followed the law of the wall closely. It is clear that the heat flux influence is dampened in the whole profile except for points below $y^+ = 30$.

Fig. 14 shows the axial turbulence intensity (u') at various values of wall heating for Re = 3309, 9929, and 16549. For the low Reynolds number (Fig.14(a)) the heat flux influence is large, even for low heat flux cases. Two trends are observed: first, from $q'' = 3.95$ to 9.02 kW/m^2 there is a decrease in the axial turbulence intensities with respect to the isothermal case, the second trend is observed for the higher heat fluxes where an increase of wall heat flux increases significantly the turbulence intensity. The axial turbulence intensity profiles for the medium Reynolds number (Re = 9929) are shown in Fig. 14(b). Two trends are observed here as well, but in this case the first trend persists for higher heat flux cases, ranging from $q'' = 3.9$ to 22.3 kW/m^2 where the profiles are seen to be below or close to the isothermal case. The starting point for the second trend is shown for wall heat fluxes larger than 35.9 kW/m^2, but a significant increase of the turbulence intensity profile is observed after reaching a wall heat flux of 48.7 kW/m^2. Fig. 14(c) shows the turbulence intensity profiles for the high Reynolds case (Re = 16549). Here the wall heat flux influence is dampened and only a small increase of the turbulence intensity profile was observed. No decrease in the axial turbulent intensity was observed below the isothermal case as in the low Reynolds case studied here.

Fig. 15 shows the normal turbulence intensity profile (v') at various values of wall heating for Re = 3309, 9929, and 16549. These figures show similar trends than those

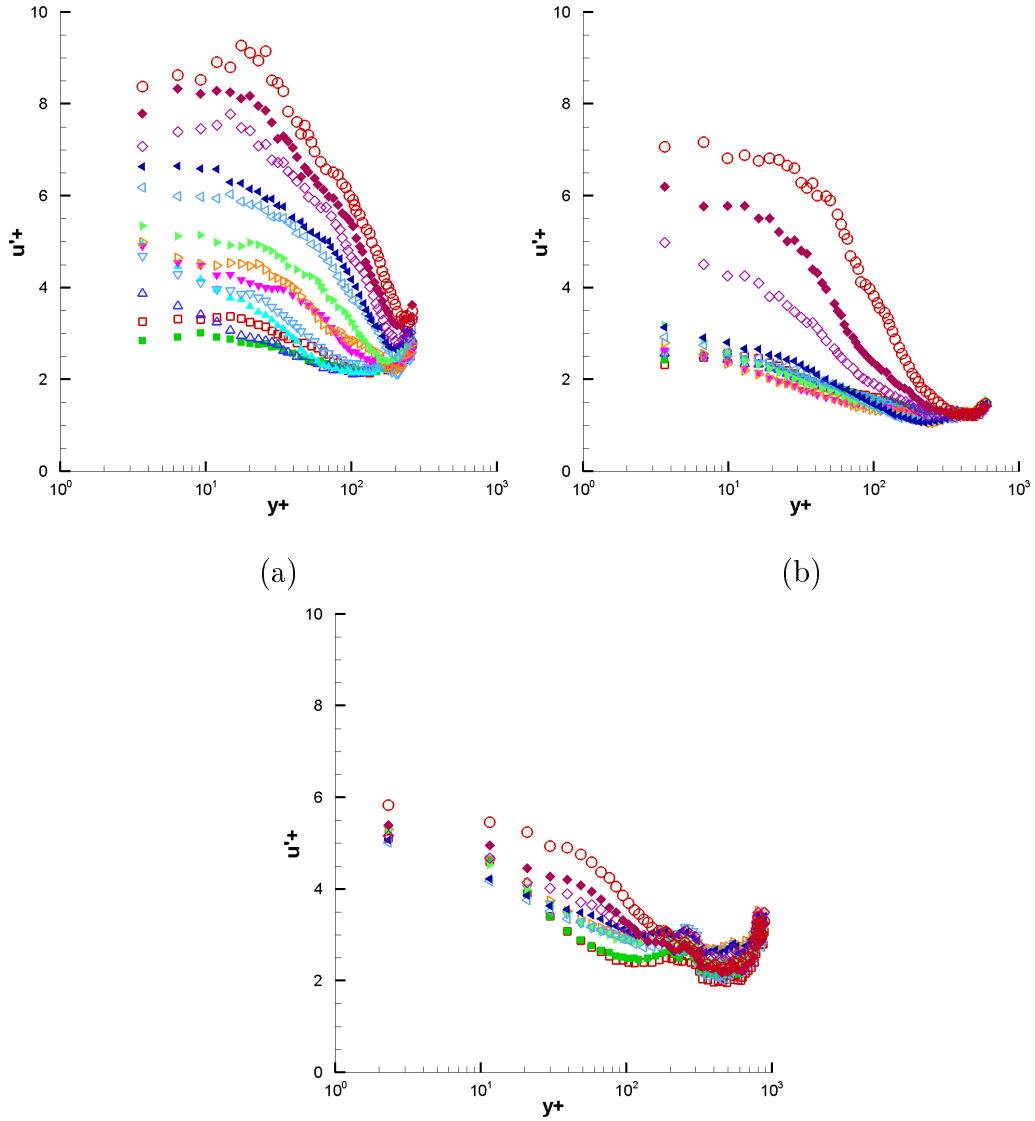

Fig. 14. Mean axial turbulence intensity profile normalized with single-phase flow friction velocity for (a) Re = 3309, u^* = 0.012 m/s, (b) Re = 9926, u^* = 0.027 m/s, (c) Re = 16549, u^* = 0.040 m/s, with q'' = 0.0 □, 3.9 ■, 9.0 △, 12.2 ▲, 16.0 ▽, 18.3 ▼, 20.3 ▷, 22.3 ▶, 35.9 ◁, 42.3 ◀, 48.7 ◊, 56.6 ⧫, 64.0 ◯ [kW/m^2]

found for the axial turbulence intensities (u'). The two trends discussed previously are observed in Fig. 15(a). The first heat flux case $q'' = 3.95$ showed a decrease on the profile compared to the isothermal case, while the rest of the heat flux cases presented a large increase on turbulence intensity due to the wall heating. Similar behavior is found for the medium and high Reynolds number however, by increasing the Reynolds number value, the wall heating influence is reduced.

The Reynolds stresses $u'v'$ profiles are shown in Fig. 16, for Re = 3309, 9929, and 16549. The wall heat flux brought significant changes on the $u'v'$ profile. In general a profile decrease tendency is found as a result of a wall heat flux increment as well as a marked shift of the zero location toward the heated wall can be observed. For the low Reynolds number (Fig. 16(a)) these changes are large. At the beginning of heating from $q'' = 3.95$ to 12.23 kW/m^2 a peak reduction and shift of the zero Reynolds stress location toward the wall is found. Further increase of the heat flux reduced the profile even more and an inverted peak is observed. The location of this inverted peak (minimum value) will shift toward the center of the channel with wall heat flux increments. The same trends are found for the medium Reynolds number (Fig. 16(b)), where the profile reduction is more clear for points up to $y^+ = 380$. For positions larger than this value, a smaller decrease is seen. The zero shifting and peak inversion is also present in this Reynolds number. For the highest Reynolds number the effect of the wall heat flux starts to be noticeable only at high q'' values. There are not significant differences in the profiles up to a heat flux value of 48.7 kW/m^2. For this Reynolds number, the zero value shifting and peak inversion influence were not noted.

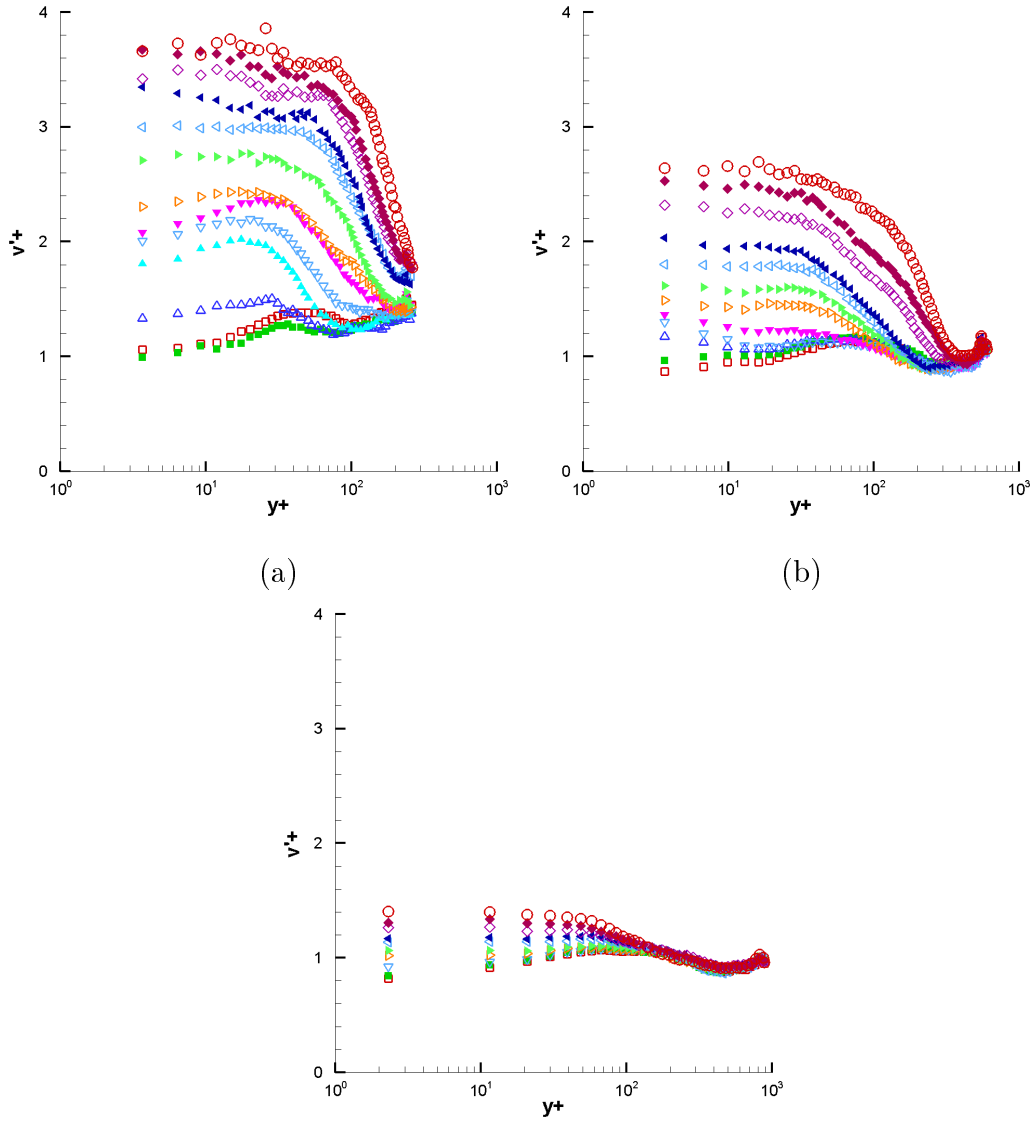

Fig. 15. Mean normal turbulence intensity profile normalized with single-phase flow friction velocity for (a) Re = 3309, u^* = 0.012 m/s, (b) Re = 9926, u^* = 0.027 m/s, (c) Re = 16549, u^* = 0.040 m/s, with q'' = 0.0 □, 3.9 ■, 9.0 △, 12.2 ▲, 16.0 ▽, 18.3 ▼, 20.3 ▷, 22.3 ▶, 35.9 ◁, 42.3 ◀, 48.7 ◊, 56.6 ⧫, 64.0 ◯ [kW/m^2]

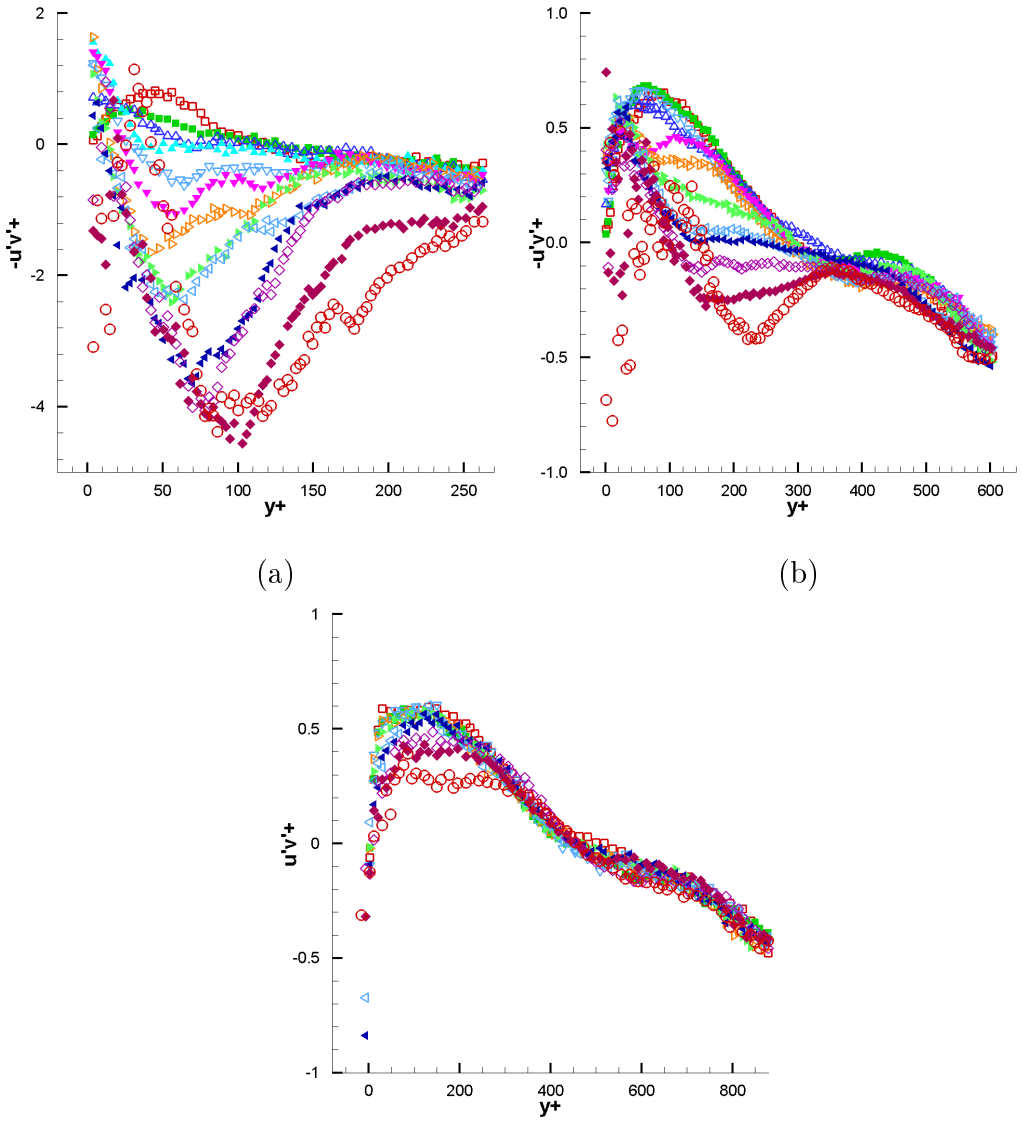

Fig. 16. Reynolds stresses profile normalized with single-phase flow friction velocity for (a) Re = 3309, $u^* = 0.012$ m/s, (b) Re = 9926, $u^* = 0.027$ m/s, (c) Re = 16549, $u^* = 0.040$ m/s, with $q'' = 0.0$ □, 3.9 ■, 9.0 △, 12.2 ▲, 16.0 ▽, 18.3 ▼, 20.3 ▷, 22.3 ▶, 35.9 ◁, 42.3 ◀, 48.7 ◊, 56.6 ⧫, 64.0 ◯ [kW/m^2]

CHAPTER VI

DISCUSSION

Some of the mechanisms that govern the fluid behavior are presented and discussed. First, the heated single-phase behavior is explored to serve as a basis to explain the further more complex mechanisms present when boiling appears. Previous works discussed the effects of buoyancy forces on the single-phase heated velocity fields (no boiling involved): According to Petuhkhov [31], buoyancy affects the flow field in a heated channel via two mechanisms. Firstly, the buoyancy force acts on the entire flow because of the non-homogeneous fluid density distribution, or the so-called *external effect.* The second effect arises from the fluctuating liquid density in the gravity field. This direct effect of buoyancy on turbulence was termed the *structural effect* [31]. The transport of momentum and thermal energy are influenced by a complicated interaction between the structural and external effects of buoyancy. In turbulent mixed convection in a vertical channel, the structural effect appears first, influencing the axial velocity in points away from the heated wall. The external effect would not be significant during phases of low Gr/Re^2. This explains the essentially unchanged mean axial velocity near the heated inner wall and a discernible effect farther from the wall (see Fig. 12(c)). By increasing the wall heat flux, the external effects are expected to become more significant leading to the well-known free convection effect of a fuller mean axial velocity profile near the heated wall. The turbulent kinetic energy in the proximity of the heated wall is not influenced by the structural effects,

at least for low Gr/Re^2[1]. For points far from the heated wall, the fluctuating buoyancy force contribution is expected to be negative, and the production term which is positive, decreases in magnitude compared to the isothermal flow. Thus, suppression of turbulence is expected for regions far from the heated wall (see the low wall heat flux cases in Fig. 14(a) to 15(c)). In this work, the turbulence suppression in regions farther from the wall, was found in all cases, except for the higher Reynolds number case ($Re = 16549$). For this case a consistent increase with wall heat flux was found. We now briefly discuss some of the physical implications of the subcooled boiling measurements.

[1] suggested that two-phase flow turbulence is the result of nonlinear interaction between wall turbulence and bubble-induced pseudo-turbulence, the latter being perturbations due to random stirring of the liquid by the bubbles and deformation of their surface. It has been conjectured that these perturbations are proportional to the local vapor fraction and the square of the vapor bubble velocity relative to the liquid, and additionally that they contribute directly to the normal Reynolds stresses only. Through dynamic interactions, they contribute to the Reynolds shear stresses. In this work, the axial Reynolds shear stress magnitude increased sharply near the inner wall, where the vapor fraction was high [2], as was the normal gradient of liquid mean axial velocity. The high vapor fraction served to diminish the production rate, whereas the high Reynolds shear stress and mean strain rate augmented the production rate in the wall vicinity. It is important to note that one feature was found in this work that was not measured or explained in previous studies. As observed by other

[1]The results of this work showed differently, even for low values of Gr/Re^2, small but significant differences of the turbulence intensities were found close to the heated wall.

[2]Void fraction measurements are provided in the next section.

researchers, at high values of Gr/Re^2, the maximum axial velocity was augmented and shifted toward the heated wall. The consistency of this behavior stopped when reaching a critical value of Gr/Re^2. At this value, the maximum axial velocity shifting toward the heated wall changed toward the center of the channel. The maximum axial velocity increased no longer with increments of the heat flux. This behavior can be clearly seen in Fig. 12(a). For high heat fluxes (high Gr/Re^2), buoyancy and bubble interaction influence over the axial velocity in the axial direction, reached a maximum. Once this point is surpassed, buoyancy and bubble interaction influence start extending in the normal direction toward the center of the channel.

CHAPTER VII

CONCLUSIONS

Using PTV, liquid velocity fields of a turbulent subcooled boiling flow in a rectangular channel were successfully obtained. The present results agree with similar studies that used point measurement probes [5, 11, 9] . However, the present study provides additional information; not only averaged profiles of the velocity components were obtained, but also instantaneous 2D velocity fields were measured with high temporal and spatial resolution. New and detailed information was obtained; specifically for the cases of low Reynolds number and high wall heat fluxes. The influence of buoyancy and bubble interaction on the axial direction reached a maximum. Further increase on the heat flux showed that the influence of buoyancy and bubble interaction extended normally to the heated wall. Both dimensional and non-dimensional data are presented with the hope that they will be useful in turbulence modeling efforts.

REFERENCES

[1] M. Lance and J. Bataille, "Turbulence in the liquid phase of a uniform bubbly air–water flow," *J. Fluid Mechanics*, vol. 222, pp. 95–118, 1991.

[2] H. Barrow, "An analytical and experimental study of turbulent gas flow between two smooth parallel walls with unequal heat fluxes," *Int. J. Heat Mass Transfer*, vol. 5, pp. 469–487, 1962.

[3] R.P. Roy, V.S. Krishnan, and A. Raman, "Measurements in turbulent liquid flow through a vertical concentric annular channel," *J. Heat Transfer*, vol. 108, pp. 216–218, 1986.

[4] A. Hasan, R.P. Roy, and S.P. Kalra, "Velocity and temperature fields in turbulent liquid flow through a vertical concentric annular channel," *Int. J. Heat Mass Transfer*, vol. 35, no. 6, pp. 1455–1467, 1992.

[5] I.N.G. Wardana, T. Ueda, and M. Mizomoto, "Structure of turbulent two-dimensional channel flow with strongly heated wall," *Exp. Fluids*, vol. 13, no. 1, pp. 17–25, 1992.

[6] V. Velidandla, S. Putta, and R.P. Roy, "Turbulent velocity field in isothermal and heated liquid flow through a vertical annular channel," *Int. J. Heat Mass Transfer*, vol. 39, pp. 3333–3346, 1996.

[7] J.A. Zarate, M. Capizzani, and R.P. Roy, "Velocity and temperature wall laws in a vertical concentric annular channel," *Int. J. Heat Mass Transfer*, vol. 41, pp. 287–292, 1998.

[8] S. Kang, B. Patil, J.A. Zarate, and R.P. Roy, "Isothermal and heated turbulent upflow in a vertical annular channel–part i. experimental measurements," *Int. J. Heat Mass Transfer*, vol. 44, no. 6, pp. 1171–1184, 2001.

[9] J.A. Zarate, R.P. Roy, and A. Laporta, "Isothermal and heated turbulent upflow in a vertical annular channel–part ii. numerical simulations," *Int. J. Heat Mass Transfer*, vol. 44, no. 6, pp. 1185–1199, 2001.

[10] R.P. Roy, A. Hasan, and S.P. Kalra, "Temperature and velocity fields in turbulent liquid flow adjacent to a bubbly boiling layer," *Int. J. Multiphase Flow*, vol. 19, no. 5, pp. 765–795, 1993.

[11] R.P. Roy, V. Velidandla, and S.P. Kalra, "Velocity field in turbulent subcooled boiling flow," *J. Heat Transfer*, vol. 119, pp. 754, 1997.

[12] T.H. Lee, G.C. Park, and D.J. Lee, "Local flow characteristics of subcooled boiling flow of water in a vertical concentric annulus," *Int. J. Heat Mass Transfer*, vol. 28, no. 8, pp. 1351–1368, 2002.

[13] R. Situ, T. Hibiki, X. Sun, Y. Mi, and M. Ishii, "Flow structure of subcooled boiling flow in an internally heated annulus," *Int. J. Heat Mass Transfer*, vol. 47, no. 24, pp. 5351–5364, 2004.

[14] F. Ramstorfer, H. Steiner, and G. Brenn, "Modeling of the microconvective contribution to wall heat transfer in subcooled boiling flow," *Int. J. Heat Mass Transfer*, vol. 51, pp. 4069–4082, 2008.

[15] R.P. Roy, S. Kang, J.A. Zarate, and A. Laporta, "Turbulent subcooled boiling flow experiments and simulations," *J. Heat Transfer*, vol. 124, pp. 73, 2002.

[16] G.H. Yeoh, J.Y. Tu, T. Lee, and G.C. Park, "Prediction and measurement of local two-phase flow parameters in a boiling flow channel," *Num. Heat Transfer, Part A*, vol. 42, no. 1, pp. 173–192, 2002.

[17] B. Končar, I. Kljenak, and B. Mavko, "Modelling of local two-phase flow parameters in upward subcooled flow boiling at low pressure," *Int. J. Heat Mass Transfer*, vol. 47, no. 6-7, pp. 1499–1513, 2004.

[18] Y.A. Hassan, C.C. Gutierrez-Torres, and J.A. Jimenez-Bernal, "Temporal correlation modification by microbubbles injection in a channel flow," *Int. Com. Heat Mass Transfer*, vol. 32, no. 8, pp. 1009–1015, 2005.

[19] E.E. Dominguez-Ontiveros, C.E. Estrada-Perez, J. Ortiz-Villafuerte, and Y.A. Hassan, "Development of a wall shear stress integral measurement and analysis system for two-phase flow boundary layers," *Rev. of Scientific Inst.*, vol. 77, pp. 105103, 2006.

[20] J. Ortiz-Villafuerte and Y.A. Hassan, "Investigation of microbubble boundary layer using particle tracking velocimetry," *J. Fluid Mechanics*, vol. 128, pp. 507, 2006.

[21] 3M, "Product information, 3M Novec 7000, engineered fluid," website: http://multimedia.mmm.com/mws/. (Accessed on April 2009).

[22] RE Canaan and YA Hassan, "Simultaneous velocity measurements of both components of a two-phase flow using particle image velocimetry," *Transactions of the American Nuclear Society*, vol. 63, 1991.

[23] C.E. Estrada-Perez, "Analysis, comparison and modification of various particle image velocimetry (PIV) algorithms," Master thesis, Texas A&M University, USA, TX, December 2004.

[24] K. Takehara, "A Study on Particle Identification in PTV Particle Mask Correlation Method," *Journal of Visualization*, vol. 1, no. 3, pp. 313–323, 1998.

[25] C.E. Willert and M. Gharib, "Digital particle image velocimetry," *Exp. Fluids*, vol. 10, no. 4, pp. 181–193, 1991.

[26] H. Noback and M. Honkanen, "Two-dimensional Gaussian regression for subpixel displacement estimation in particle image velocimetry or particle position estimation in particle tracking velocimetry," *Exp. Fluids*, vol. 38, no. 4, pp. 511–515, 2005.

[27] K. Okamoto, S. Nishio, T. Saga, and T. Kobayashi, "Standard images for particle image velocimetry," *Meas. Sci. Technol.*, vol. 11, pp. 685–681, 2000.

[28] S.J. Kline and F.A. McClintock, "Describing uncertainties in single-sample experiments," *Mec. Eng.*, vol. 75, no. 1, pp. 3–8, 1953.

[29] M.L. Riethmuller, *Particle image velocimetry and associated techniques*, Von Karman Institute for Fluid Dynamics, Rhode St. Genese, Belgium, 2000.

[30] I.N.G. Wardana, T. Ueda, and M. Mizomoto, "Effect of strong wall heating on turbulence statistics of a channel flow," *Exp. Fluids*, vol. 18, no. 1, pp. 87–94, 1994.

[31] B.S. Petukhov and A.F. Polyakov, *Heat transfer in turbulent mixed convection*, Hemisphere Publishing Corporation, Washington, USA, 1988.

[32] G. E. Elsinga, B. W. van Oudheusden, and F. Scarano, "Evaluation of aero-optical distortion effects in PIV," *Experiments in Fluids*, vol. 39, no. 2, pp. 246–256, 2005.

APPENDIX A

MEASUREMENTS UNCERTAINTIES

A. Flow Meter Correction

In this work, a variable area flow-meter model F-450 from Blue-White industries, was used. The full-scale accuracy accounts for +/–5%.

Since the flow-meter calibration accounted only for water, a calibration correction was needed because HFE-7000 3M Refrigerant was used on the PTV experiments. The flow meter calibration correction is given by

$$\dot{Q}_C = \dot{Q}_M \times 0.6842$$

Where $\dot{Q}_C$ and $\dot{Q}_M$ are the corrected and the measured volumetric flow rates. Using the unheated single-phase PTV experimental results, the previous flow-meter correction was tested. The flow-meter measurement was $\dot{Q}_M = 3.79 \times 10^{-5}\ m^3/s$, then the corrected volumetric flow rate is $\dot{Q}_C = 2.59 \times 10^{-05}$ m^3/s, with this value an average axial velocity was estimated with

$$\overline{V}_{FM} = \frac{\dot{Q}_C}{A_f}]$$

Where A_f is the flow area equal to 6.61×10^{-5} m ^{2}. Substituting values the average velocity obtained from the flow-meter is $\overline{V}_{FM} = 0.39$ m/s.

The average velocity calculated from the PTV experimental data is defined as

$$\overline{V}_{PTV} = \frac{1}{H}\int_0^H u(y)dy \tag{A.1}$$

Where H is the channel height equal to $8.7 \times 10^{-3}\, m$, and $u(y)$ is the axial velocity profile obtained from the spatial-temporal average of 5000 velocity fields from the PTV experiment. The experimental data points were fitted with equation (A.3) with a goodness of fit of $R^2 = 0.987$. Fig. 17 shows the experimental liquid velocity profile and the corresponding fitted curve.

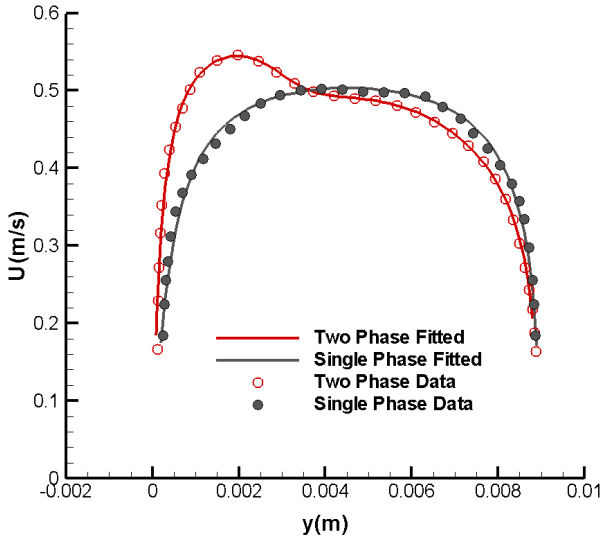

Fig. 17. Mean axial liquid velocity profiles and fitted curves for single and two-phase flow (q'' =56.6 kW/m^2) at a $Re = 9929$

Using equations (A.3) and (A.1) we obtain an average axial velocity of $\overline{V}_{PTV} = 0.4402\, m/s$. From this results, the relative error between $\bar{V}_{FM}$ and $\bar{V}_{PTV}$ accounts for about 10%

The average axial velocity ($\overline{V}$) was estimated successfully with two different techniques, directly from the flow meter ($\bar{V}_{FM}$) and indirectly form the PTV measurements ($\overline{V}_{PTV}$). PTV estimation was about 10% larger. The reason of this discrepancy is

attributed to the fact that the PTV measurements were acquired in the center plane of the channel where the maximum velocity is located, if PTV measurements on more planes were available, this discrepancy should decrease.

B. Mass Conservation Validation

In this section the liquid mass conservation principle is used to validate the PTV measurements of the axial velocity profile for single and two-phase flow cases. From the PTV results the effect of the heat flux over the axial velocity profile is clear, for high heat fluxes when boiling is present there is an increase on the velocity for regions close to the heated wall, while for regions far from the heated wall the velocity decreases (See Fig. 17). Assuming low void fractions and that the liquid mass flow rate entering the test section was maintained constant, the curve of the two-phase liquid velocity profile must be close to that of single-phase liquid velocity profile, or

$$\dot{m}_{l_{SP}} = \rho_l b \int V_{SP}(y)dy \approx \dot{m}_{l_{TP}} = \rho_l b \int V_{TP}(y)dy \tag{A.2}$$

Where $\dot{m}_{l_{SP}}$ is the mass flow rate in the single-phase condition, $\dot{m}_{l_{TP}}$ is the mass flow rate of the two-phase case, $V_{SP}(y)$ and $V_{TP}(y)$ represents the liquid velocity profiles of the single-phase and two-phase cases respectively, and b is the channel width. Fig. 17 shows the axial liquid velocity profiles obtained from the PTV results for the non heated case (single-phase flow) and the heated case (two-phase flow) with a wall heat flux of $q''_w = 66.6$ kW/m^2, both at a Reynolds number of $Re = 9929.82$. The data points were fitted by polynomial curves, with goodness of fit values of $R^2 = 0.987$ and 0.978 respectively. The fitted curve equation for the single-phase case is given by

$$V_{SP}(y) = \frac{ab + cby + eby^2 + gby^3}{1 + bby + dby^2 + fby^3} \tag{A.3}$$

with constants given by: ab=-0.029710, bb=2354.870, cb=1481.253, db=-5.393·10^5, eb=-3.240·10^5, fb=2.948·10^7, gb=1.775·10^7. The fitted curve equation for the two-phase case is given by

$$V_{TP}(y) = \frac{aa + cay + eay^2 + gay^3 + iay^4 + kay^5}{1 + bay + day^2 + fay^3 + hay^4 + jay^5} \tag{A.4}$$

with constants given by: aa=0.008211, ba=4319.088, ca=3133.339, da=-3.403·10^6, ea=-2.271·10^6, fa=9.513·10^8, ga=6.212·10^8, ha=-1.045·10^{11}, ia=-6.935·10^{10}, ja=3.869·10^{12}, ka=2.673·10^{12}. Using equations (A.2) and (A.3) and assuming the same liquid density ($\rho = 1400$ kg/m^3)[1] and same liquid flow area ($A_\perp = b \cdot \int dy$, with $b = 7.6$ mm and dy from 0 to 8.7 mm), we obtain $\dot{m}_{l_{SP}} = 0.0437$ kg/s. Similarly using equations (A.2) and (A.4) we obtain $\dot{m}_{l_{TP}} = 0.0419$ kg/s.

From the previous results a mass flux relative difference of 3.9% is found. This confirms that the procedures of phase discrimination (identifying liquid from gas) and liquid velocity estimation was successful. It is important to note that further corrections are needed; for instance the density changes on the heated case was not considered on the calculation, neither the effect of the small void fraction close to the wall.

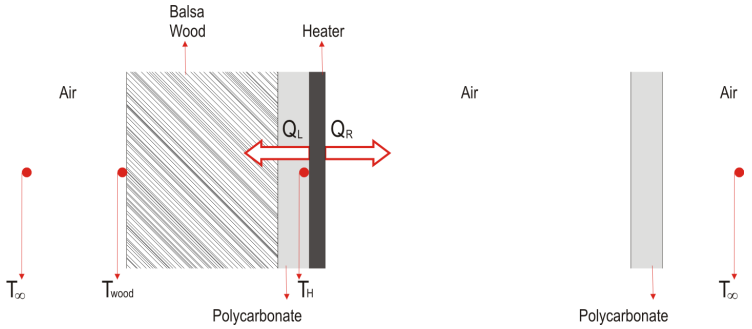

Fig. 18. Simplified test sections schematics to estimate heat losses (not on scale).

C. Heat Loss Estimation

To estimate the heat losses an energy balance is conducted using the system shown in Fig. 18. For sake of simplicity this system is considered one dimensional with a heat loss (Q_{Loss}) equal to the heat transferred through the left face of the heater (Q_L). The heat loss conduction resistances are due to the insulation from the thin polycarbonate wall (0.7 mm) and the thick layer of balsa wood ($13mm$), similarly the heat transferred through the right heater wall (Q_R) faces a resistance from the thin polycarbonate wall (0.7 mm) and by the thick layer of air (8.7 mm) inside the channel. The test section inlet and outlet valves were closed to limit the inside air movement therefore reducing convective heat transfer. Thermocouples were used to measure: a) the heater outside wall temperature (left heater wall) at six different heights ($T_{H,1}$, $T_{H,2}$, ...$T_{H,6}$), b) the ambient air temperature (T_∞), and c) the outside insulation wall temperature (T_{wood}) (the left balsa wood wall).

[1]Strictly speaking, the density must be different in both cases, but since we are working on subcooled conditions and with the liquid phase only, this assumption can be accepted.

Energy was supplied to the heater (Q_H) by a DC power source from which direct measurements of the current (I) and the voltage (V) are available. The energy transferred to the heater was calculated using

$$Q_H = A \times V \tag{A.5}$$

The heat transfer to the heater ranged from 2.01 to 13.72 W. No larger power values were used to avoid heater damage. Table II shows the different heater power conditions for each experiment.

Table II. Experimental conditions

Experiment	Current $[Amps]$	Voltage $[Volts]$	Q_H $[W]$
1	0.28	7.20	2.01
2	0.40	10.40	4.16
3	0.47	13.00	6.11
4	0.60	16.30	9.78
5	0.70	19.60	13.72

For each new condition three hours were used as a steady state waiting time, after which, temperature measurements[2] were acquired for 100 s at a rate of 100 Hz.

From the thermal circuit shown in Fig. 19, the heat loss can be expressed as:

[2]Thermocouple $T_{H,6}$ measurements were neglected due to its large variation with respect to the other thermocouples.

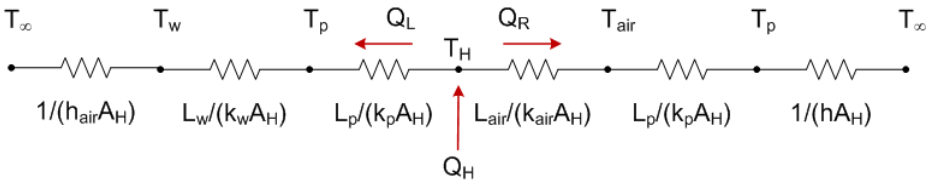

Fig. 19. Thermal circuit of the system

$$Q_{Loss} = Q_L = \frac{(\overline{T}_H - T_w)}{\frac{L_p}{k_p A_H} + \frac{L_w}{k_w A_H}} \tag{A.6}$$

Where $\overline{T}_H$ is the average heater wall temperature, T_w is the balsa wood left wall temperature, L_p and L_w are the polycarbonate and balsa wood wall thicknesses, k_p and k_w are the thermal conductivities of the polycarbonate and the balsa wood wall, A_H is the heater area. Also assuming a value for the convective heat transfer coefficient for air outside the test section (h_∞), the heat loss can be expressed in terms of the air ambient temperature (T_∞) as

$$Q_{Loss} = Q_L = \frac{(\overline{T}_H - T_\infty)}{\frac{L_p}{k_p A_H} + \frac{L_w}{k_w A_H} + \frac{1}{h_\infty A_H}} \tag{A.7}$$

Using the system dimensions, temperatures and the following properties $h_\infty = 16.7$ W/m^2K $k_p = 0.2$ W/mK $k_w = 0.055$ W/mK the estimation of Q_{Loss} calculated with equations (A.6) and (A.7) have a maximum relative difference of about 3.6% confirming the goodness of the selected material properties values. Fig. 20 shows the heat loss estimated by this two equations as a function of the heat transferred to the heater.

From the previous analysis, a heat loss calibration plot is obtained, and is shown in Fig. 21. The percentage of system heat loss is a function of the temperature

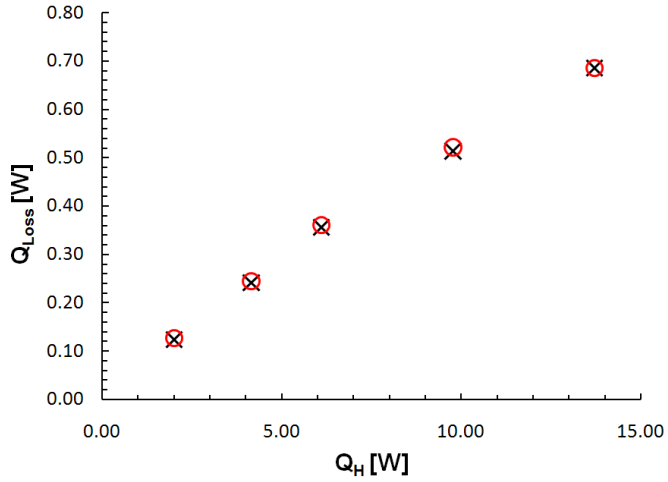

Fig. 20. Heat loss Q_{Loss} as a function of the heat transferred to the heater Q_H calculated using: equation A.6 ○, equation A.7 ×.

difference $(T_H - T_\infty)$. For example, for one temperature difference condition of 50 °C between the heater surface and the ambient had a corresponding percentage of heat loss of about 6.2%. The heat loss data is then used in calculating the actual heat carried away by the refrigerant flowing in the test section.

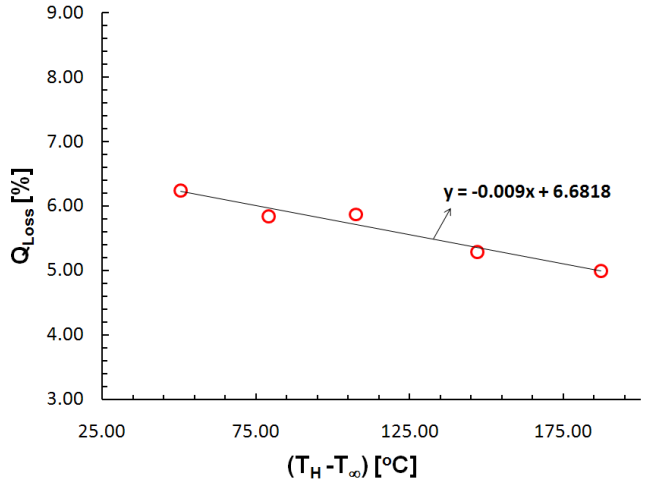

Fig. 21. Percentage of heat loss as a function of the temperature difference $(T_H - T_\infty)$

D. Influence of Visualization Devices on the Heat Transfer of the System

This section describes the experiments used to quantify the heat transfer modification inherent of the visualization techniques devices, namely: due to PIV particles ($\dot{Q}_{Particles}$), halogen lamp light, ($\dot{Q}_{Halogen}$) and laser light ($\dot{Q}_{Laser}$). The fluid turbulence modification due to changes on heater power can not be correctly assessed if there is not an estimate of the additional heat provided by the flow visualization devices, therefore convective boiling experiments with $Re = 9929.82$ and heater power values (Q_H) of 0.0, 4.98, 15.13, 45.42, and 80.56 W were performed considering four different cases: a) reference (with no visualization devices), b) fluid with PIV particles, c) fluid with halogen lamp illumination, and d) fluid with laser illumination. In these experiments three hours were used as a steady state waiting time, after which, temperature measurements were acquired for 10 s at a rate of 2000 Hz. In these experiments were measured the heater wall temperature at different heights, the channel inlet and outlet fluid temperatures and the ambient air temperature. To quantify the influence of the illumination devices on the heat transfer problem, the heater wall temperatures and the heat gained by the fluid in each case is analyzed and compared. Fig. 22 shows a graphical comparison of the heater wall temperatures for the different cases. The maximum relative and absolute differences were computed for each case, and are shown in Table III, it is clear that there are not noticeable differences on the measured temperatures.

The heat gained by the fluid in the test section is proportional to the difference between the channel outlet and inlet fluid temperatures (ΔT_f). This temperature differences can help as an indicator of whether or not the illumination devices are introducing significant heat to the system. In Fig. 23 are shown the effects of the illumination devices over ΔT_f for different heater powers. Comparing to the reference

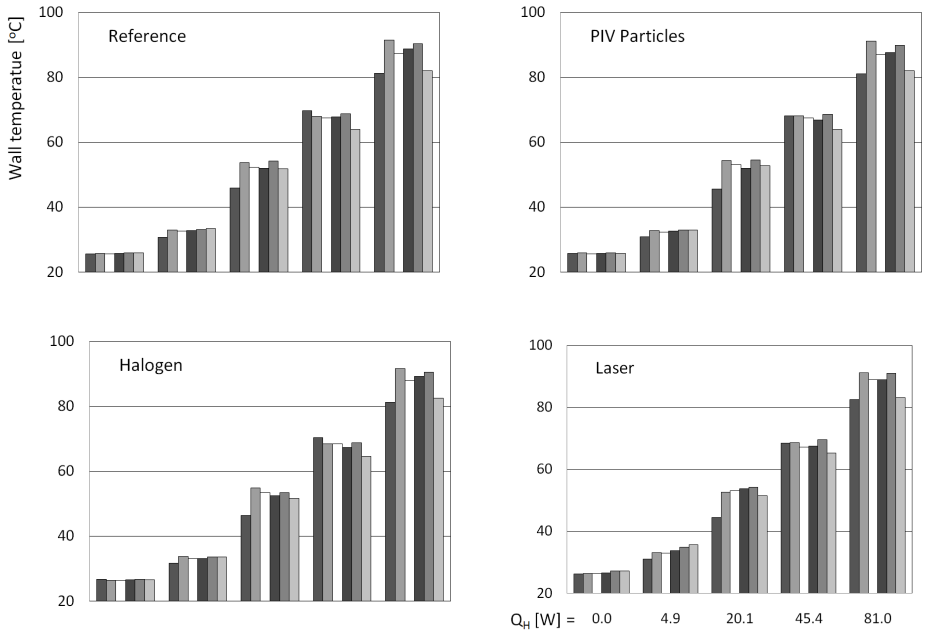

Fig. 22. Wall temperature comparison for different cases. Temperature measured with thermocouples $T_{H,1}$ ■, $T_{H,2}$ ■, $T_{H,3}$ □, $T_{H,4}$ ■,$T_{H,5}$ ■, $T_{H,6}$■.

Table III. Maximum relative and absolute wall temperature differences with respect to the reference case.

Device	Relative Difference %	Absolute Difference [°C]
PTV particles	2.23	1.56
Halogen lamp	4.11	1.09
PTV laser	6.53	2.18

values (with no illumination devices), it is clear that the effect of the illumination devices over the energy gained by the fluid is also negligible, having a maximum absolute difference value of 0.15 ℃.

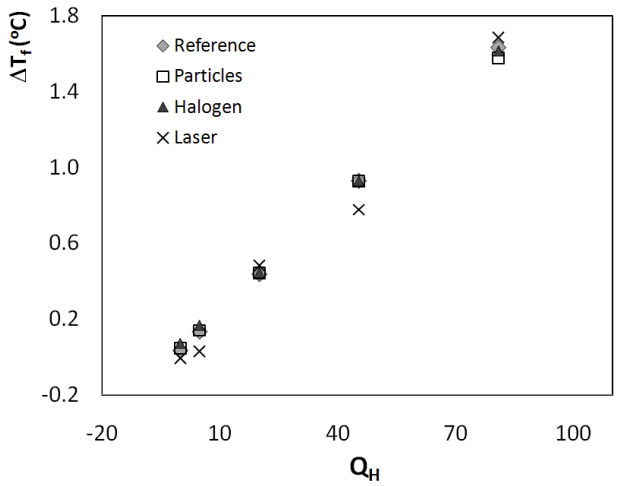

Fig. 23. Differences between channel outlet and inlet fluid temperatures measured for each different illumination case for different heater powers.

Considering that the thermocouples errors accounts for 2.2 ℃or 0.75% of the measured temperature. It can be concluded that the effect of the illumination devices on the overall heat transfer of the system is negligibly small and within the values of the thermocouple errors. Further investigations are needed to determine the local effects induced by these devices.

E. Aero-Optical Distortion Effects in the PTV Measurements

Most of the following analysis is based on the work of Elsinga et. al. [32] on which is explained that errors due to optical distortion effects are expected when using image visualization techniques such as PIV and PTV through in-homogeneous flows.

Distortion of the imaging process occurs if the illuminated particles are observed through an optically inhomogeneous medium, as in the case of compressible flows, shear layers and thermal convection flows. The resulting image of the particle image pattern is subjected to deformation and individual particles may be perceived as blurred [32]. In relation to PIV and PTV two forms of error can be identified: position error and velocity error. The position and velocity error are a direct consequence of the geometrical deformation of the image, which results in a systematic (bias) error of the measured velocity. In synthesis one may say that the wrong velocity vector is evaluated at the wrong position. Image blur affects the tracking precision in terms of cross-correlation accuracy due to the (anisotropic) increase of the particle image size, thus broadening the correlation peak. In the following discussion, the emphasis is given to the characterization of errors.

For this analysis, it is assumed steady state flow, ideal imaging, ideal tracking, negligible pixelization effects, no particle lag, and, no magnification effects. The particle velocity $\vec{V}_p$ and the image distortion, which is related to the flow density field, depend only on the spatial location in the imaging plane. After a light ray coming from a particle in the PIV measurement plane has left the refractive index field in the test section, it propagates along a straight line. A linear backward extension of that line to the plane of focus provides the position at which that particle is perceived by the imaging system. Fig. 24(left) shows an undisturbed light ray propagating through a homogeneous refractive index field and the disturbed one (through an inhomogeneous refractive index field), coming from a single particle and initially propagating in the same direction. A backward extension of the two light rays (dashed line) reveals that for the disturbed light ray, the imaged position of the particle (open circle) is different from the actual position of the particle in the PIV plane (solid circle).

This spatial displacement is referred to as the position error. Fig. 24(right) shows a single particle (moving to the right) at two subsequent exposures separated by a time interval Δt. The position error at the two spatial locations may differ returning different position errors for the two particle images. This results in an error in the particle image displacement, hence measured particle velocity. This is referred to as the direct velocity error.

1. Particle Position Error

The image distortion can be expressed in terms of an optical displacement vector $\vec{\xi}(\vec{x}_p(t))$, as:

$$\vec{\xi}(\vec{x}_p(t)) = \vec{x}'_p(t) - \vec{x}_p(t) \tag{A.8}$$

where $\vec{x}_p(t)$ is the actual particle location (x, y) in the measurement plane and $\vec{x}'_p(t)$ is the location where that particle is perceived. The optical displacement vector is directly equivalent to the position error of the measurement and is related to the gradient of the refractive index ∇n. The optical displacement vector based on the theory of light propagation in a refractive index field is

$$\vec{\xi}(\vec{x}) = -Z_D\vec{\epsilon}(\vec{x}) = -Z_D \int_S \nabla n(\vec{x}, z)dz \tag{A.9}$$

where z is the coordinate direction normal to the PIV measurement plane, ϵ is the light beam deflection angle and Z_D is the distance parallel to the optical axis between the measurement plane and the intersection point of the disturbed ($\nabla n \neq 0$) and undisturbed ($\nabla n = 0$) light rays coming from the same particles.

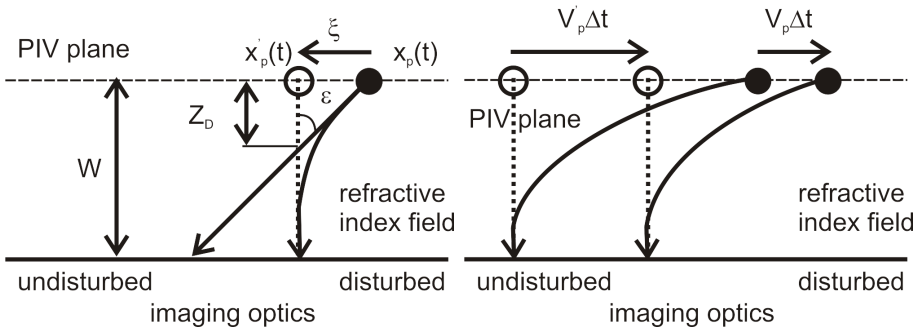

Fig. 24. Optical distortion in PTV: position error (left) and direct velocity error (right). Solid lines represent light ray trajectories coming from the particle (solid circle). Dashed lines are the backward extension of those rays indicating the position where the particle is perceived in the PIV plane (open circles)

2. Velocity Error

The velocity error is obtained following a Lagrangian approach to the tracking of a particle (image), the particle velocity $\vec{V}_p'$ is related to the particle displacement in time as:

$$\vec{V}_p(\vec{x}_p(t)) = \frac{d\vec{x}_p}{dt} \tag{A.10}$$

The observed or measured particle velocity $\vec{V}_p'$, obtained from the optically distorted images is then given by

$$\vec{V}_p'(\vec{x}_p'(t)) = \frac{d\vec{x}_p'}{dt} \tag{A.11}$$

The velocity error of the measurement is now defined as the difference between the measured velocity and the actual particle velocity at a given location $\vec{x}$ in the image:

$$\Delta\vec{V}_p'(\vec{x}_p) = \vec{V}_p'(\vec{x}_p') - \vec{V}_p(\vec{x}_p) \tag{A.12}$$

Using equations (A.10), (A.11) and substituting the optical displacement vector (Eq. A.9) and further evaluation yields

$$\Delta\vec{V}_p'(\vec{x}) = (\nabla\vec{\xi})\vec{V}_p - (\nabla\vec{V}_p)\vec{\xi} \tag{A.13}$$

The first term represents the direct velocity error (Fig. 24(right)), which is given by the product of the actual particle velocity and the gradient of the optical displacement vector. The latter represents a local change in optical magnification, which "stretches" the imaged object with respect to the physical dimension in the measured plane. The second term in Eq. A.13 is the product of the optical displacement vector with the gradient of the actual particle velocity and represents the contribution of the position error to the velocity error. Note that only the derivative of the optical displacement vector taken in the direction of the velocity vector contributes to the first term of the velocity error. It was shown previously that the optical displacement vector is related to the gradient of the refractive index (Eq. A.9).

3. Two Dimensional Flow Hypotheses

The 2D hypotheses allows simplifying the model equations for optical distortion significantly. In the assumption that the gradient of refractive index is independent of z (2D flow) the light ray trajectory is approximated by a parabola, in which case Z_D can be taken as $W/2$. The expression for the optical displacement vector (Eq. A.9) then reduces to:

$$\vec{\xi}(\vec{x}) = -\frac{1}{2}W^2\nabla n(\vec{x}) \tag{A.14}$$

Using this result, the gradient of the optical displacement vector in Eq. A.13 is given by:

$$\nabla\vec{\xi}(\vec{x}) = -\frac{1}{2}W^2\nabla^2 n(\vec{x}) \tag{A.15}$$

4. Boiling Experiments Optical Distortion Error Analysis

Using the assumption of two dimensionality, and the fact that for the boiling experiments the change of refractive index is normal to the heater wall (y direction), equation A.14 simplifies to

$$\xi_y = -\frac{1}{2}W^2\frac{dn}{dy} \tag{A.16}$$

also the first term of the velocity error (direct velocity error, Eq. A.13) cancels out and only the position error remains. The velocity error is then given by:

$$\Delta v(y) = -\frac{dv}{dy}\xi_y \tag{A.17}$$

Since dn/dy is not directly know for the refrigerant HFE-7000 a relationship relating the refractive index and the temperature is used. It is assumed that the change of refractive index as a function of temperature is given by:

$$\frac{dn}{dT} = -0.00045\frac{1}{^oC} \tag{A.18}$$

This equation is a good approximation for most organic compounds, Therefore:

$$\frac{\partial n}{\partial y} = \left(-0.00045\frac{1}{^oC}\right)\frac{dT}{dy} \approx \left(-0.00045\frac{1}{^oC}\right)\frac{\Delta T}{\Delta y} \tag{A.19}$$

Assuming the maximum value for $\Delta T = T_{sat} - T_{bulk}$ with T_{sat} = 34 ℃ and $T_{bulk} = T_{in} - T_{out}$ = 27.05 ℃ (obtained from experimental measurements) then ΔT = 6.95℃. Considering Δy as half height of the channel = 4.3 mm, and considering W =

3.8mm (distance from measurement area position to the channel wall), the maximum optical displacement error is $\xi_{y_{max}} = 5.25\mu$ m or 0.43 pixels.

The velocity error can be expressed as:

$$\Delta v(y) = \frac{dv}{dy}\xi_y \approx \frac{\Delta v}{\Delta y}\xi_y \tag{A.20}$$

Again, Δy = half height of the channel = 4.3 mm and Δv is obtained from experimental values to be $\Delta v \approx 0.01\, m/s$. then a maximum velocity error value is estimated to be $\Delta v_{max} = 12.2\, \mu m/s$ or $0.99\, pixels/s$. This error represents about 0.12% of the normal velocity, and about 0.006% of the axial velocity.

VITA

Name Carlos Eduardo Estrada Pérez

Address Texas A&M University
Department of Nuclear Engineering
3133 TAMU
College Station, TX 77843-3133

E-mail cperez@ne.tamu.edu

Education Bachelor of Science in Energy Engineering
Universidad Autónoma Metropolitana
Mexico City, Mexico, 2000.

Master of Science in Mechanical Engineering
Texas A&M University
College Station, TX, 2005.